

Scale invariance during bacterial reductive division observed by an extensive microperfusion system

Takuro Shimaya,^{1,*} Reiko Okura,² Yuichi Wakamoto,² and Kazumasa A. Takeuchi^{1,3,†}

¹*Department of Physics, Graduate School of Science, University of Tokyo, Tokyo 113-0033, Japan*

²*Department of Basic Science, Graduate School of Arts and Sciences, University of Tokyo, Tokyo 153-8902, Japan*

³*Department of Physics, School of Science, Tokyo Institute of Technology, Tokyo 152-8551, Japan*

(Dated: November 21, 2021)

In stable environments, cell size fluctuations are thought to be governed by simple physical principles, as suggested by recent finding of scaling properties. Here we show, using *E. coli*, that the scaling concept also emerges with respect to cell size fluctuations under abrupt starvation, even though the distribution changes with time. We develop a microfluidic device for observing dense and large bacterial populations, under uniform and switchable conditions. Triggering bacterial reductive division by abruptly switching to non-nutritious medium, we find that the cell size distribution changes in a specific manner that keeps its normalized form unchanged; in other words, scale invariance holds. We also find that the normalized distribution depends slightly on the growth condition before starvation. These findings are underpinned by simulations of a model based on cell growth and cell cycle. We also formulate the problem theoretically and propose a sufficient condition for the scale invariance. Finally, we numerically show the range of validity of the scale invariance over various characteristic times of the starvation process, revealing the number of multifork replications is crucial for the scale invariance. Our results emphasize the importance of intrinsic cellular cycle processes in this problem, suggesting different distribution trends for bacteria and eukaryotes.

I. INTRODUCTION

Recent studies on microbes in the steady growth phase suggested that the cellular body size fluctuations may be governed by simple physical principles. For instance, Giometto *et al.* [1] proposed that size fluctuations of various eukaryotic cells are governed by a common distribution function, if the cell sizes of a given species are normalized by their mean value (see also [2]). In other words, the distribution of cell volumes v , $p(v)$, can be described as follows:

$$p(v) = v^{-1}F(v/V), \quad (1)$$

with a function $F(\cdot)$ and $V = \langle v \rangle$ being the mean cell volume. This property of distribution is often called scale invariance. Interestingly, this finding can account for power laws of community size distributions, i.e., the size distribution of all individuals regardless of species, which were observed in various natural ecosystems [3, 4]. Scale invariance akin to Eq. (1) was also found for bacteria [5, 6] for each cell age, and the function $F(\cdot)$ was shown to be robust against changes in growth conditions such as the temperature.

Those results, as well as theoretical models proposed in this context [1, 7], have been obtained under steady environments, for which our understanding of single-cell growth statistics has also been significantly deepened recently [8–10]. By contrast, it is unclear whether such a simple concept as scale invariance is valid under time-dependent conditions, where different regulations of cell

cycle kinetics may come into play in response to environmental variations. In particular, when bacterial cells enter the stationary phase from the exponential growth phase, they undergo reductive division, during which both the typical cell size and the amount of DNA per cell decrease [11–14]. Although this behavior itself is commonly observed in test tube cultivation, little is known about single-cell statistical properties during the transient. The bacterial reductive division is therefore an important stepping stone for studying cell size statistics under time-dependent environments and understanding the robustness of the scale invariance against environmental changes.

It has been, however, a challenge to observe large populations of bacteria under uniform yet time-dependent growth conditions. For steady conditions, the Mother Machine [15], which allows for tracking of bacteria trapped in short narrow channels, was proved to be a powerful tool for measuring cell size statistics. In such experiments, the channel width needs to be adapted to cell widths in a given condition, and this renders the application to time-dependent conditions difficult. If we enlarge the channels, depletion of nutrients in deeper regions of the channels induces spatial heterogeneity, as discussed in ref.[16, 17] and later in this article. Hence, it is also required to develop a system that can uniformly control non-steady environments and give a sufficient amount of single-cell statistics with high efficiency.

In this study, we establish a novel microfluidic device, which we name the “extensive microperfusion system” (EMPS). This system can trap dense bacterial populations in a wide quasi-two-dimensional region and uniformly control the culture condition for a long time. We confirm that bacteria can freely swim and grow inside, and evaluate the uniformity and the switching efficiency

* t.shimaya@noneq.phys.s.u-tokyo.ac.jp

† kat@kaztake.org

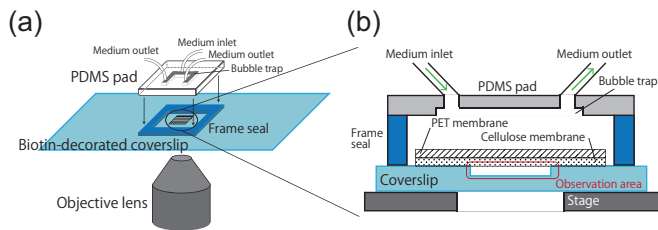


FIG. 1. Sketch of the extensive microperfusion system (EMPS). (a) Entire view of the device. Microwells are created on a glass coverslip. We attach a PDMS pad on the coverslip with a square frame seal to fill the system with liquid medium. (b) Cross-sectional view inside the PDMS pad. A PET-cellulose bilayer porous membrane is attached via the biotin-streptavidin bonding.

of the culture condition. Then we use this system for quantitative observations of bacterial reductive division processes, triggered by abrupt switching to non-nutritious medium. We observe *Escherichia coli* cells and find that the distribution of cell volumes, collected irrespective of cell ages, maintain the scale invariance as in Eq. (1) at each time, with the mean cell size that gradually decreases. On the other hand, the normalized distribution function F is found to depend on the growth condition before starvation, slightly but significantly. To obtain theoretical insights on these experimental findings, we devise a cell cycle model describing reductive division processes, by extending the Cooper-Helmstetter model [18–20] for steady growth environments. We numerically find that this model indeed shows the scale invariance under starvation conditions, confirming the robustness of this property. We also provide theoretical descriptions on the time evolution of the cell size distribution, and propose a condition for the scale invariance. Finally, we numerically show the range of validity of the scale invariance over various characteristic times of the starvation process, revealing the number of multifork replications is crucial for the scale invariance.

II. RESULTS

A. Development of the extensive microperfusion system

In order to achieve uniformly controlled environments with dense bacterial suspensions, we adopt a perfusion system as developed in ref. [21]. This system allows for supplying fresh medium through a porous membrane attached over the entire observation area, instead of supplying from an open end as polydimethylsiloxane (PDMS)-based systems usually do. In its prototypical setup, bacteria are confined in microwells made on a coverslip, covered by a cellulose porous membrane attached to the coverslip via biotin-streptavidin bonding. The pore size of the membrane is chosen so that it can confine bacteria

and also that it can exchange nutrients and waste substances across the membrane. To continuously perfuse the system with fresh medium, a PDMS pad with a bubble trap is attached above the membrane by a two-sided frame seal (Fig. 1(a) and Fig. S1(a)). This setup can maintain a spatially homogeneous environment for cell populations in each microwell, in particular if the microwells are sufficiently shallow so that all cells remain near the membrane. However, because the soft cellulose membrane may droop and adhere to the bottom for wide and shallow microwells, the horizontal size of such quasi-two-dimensional microwells has been limited up to a few tens of micrometers, preventing from characterization of the instantaneous cell size distribution.

By the EMPS, we overcome this problem and realize quasi-two-dimensional wells sufficiently large for statistical characterization of cell populations. This is made possible by introducing a bilayer membrane, where the cellulose membrane is sustained by a polyethylene terephthalate (PET) porous membrane via biotin-streptavidin bonding (Fig. 1(b), Fig. S1(b) and Appendix A). Because the PET membrane is more rigid than the cellulose membrane, we can realize extended area without bending of the membrane. Specifically, in our setup with circular wells of $110 \mu\text{m}$ diameter and $1.1 \mu\text{m}$ depth, although a cellulose membrane alone is bent and adheres to the bottom of the well (Fig. S1(c) and Movie S1), our PET-cellulose bilayer membrane keeps flat enough so that bacteria can freely swim in the shallow well (Fig. S1(d) and Movie S2). The EMPS can realize such observations for a long time with little hydrodynamic perturbation by medium flow and no mechanical stress, which may exist in a PDMS-based device that holds cells mechanically. We also check whether the additional PET membrane may affect the growth condition of cells, by using *E. coli* MG1655 and M9 medium with glucose and amino acids (Glc+a.a.). We find that the doubling time of the cell population is 59 ± 10 min, which is comparable to that in the previous system without the PET membrane [21–23]. Therefore, our bilayer membrane can still exchange medium efficiently.

We then test the spatial uniformity of the culture condition. We design U-shape traps with an open end, for both the EMPS (Fig. 2(a) and for the conventional PDMS-based device (Fig. S2(a),(b)). With this geometry, nutrients are supplied via diffusion from the open end in the PDMS-based system, while nutritious medium is directly and uniformly delivered through the membrane above the trap in the EMPS. When we culture *E. coli* MG1655 in M9(Glc+a.a.), the trap is eventually filled with cells, and they exhibit coherent flow toward the open end due to the cell growth and proliferation (Fig. 2(b) and Movie S3,4). To evaluate the uniformity of the cell growth, we measure the velocity field of the cell flow by particle image velocimetry (PIV) (Fig. S2(c),(d)). The velocity component along the stream-wise direction (the y axis in Fig. 2(b)) averaged over the span-wise direction (the x axis), $u(y) = \langle u(x,y) \rangle_x$, clearly shows that the

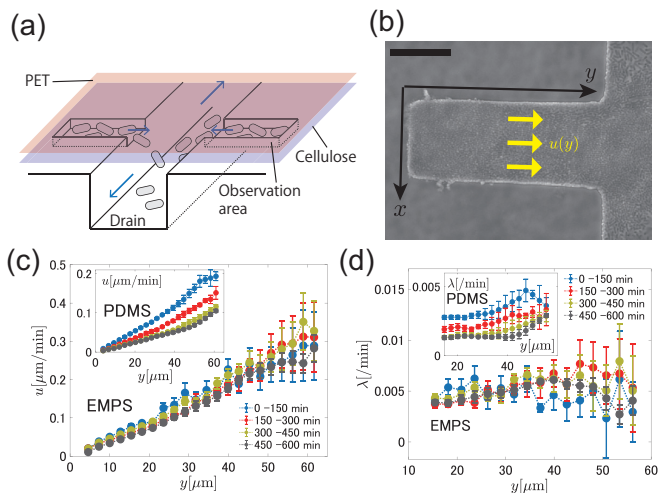


FIG. 2. Cell growth measurements in U-shape traps in EMPS. (a) Sketch of the design of microchannels. Non-motile cells are trapped in the shallow observation area. Cells in the trap can escape to the deep drain channel. (b) Top view of the trap ($30 \mu\text{m} \times 80 \mu\text{m}$, $1.0 \mu\text{m}$ depth) filled with *E. coli* W3110 $\Delta\text{fliC} \Delta\text{flu} \Delta\text{fimA}$ (see also Movie S4). The scale bar is $25 \mu\text{m}$. Coherent flow of cells driven by cell proliferation is directed toward the drain ($15 \mu\text{m}$ depth). (c) The stream-wise (y) component of the velocity field averaged over the span-wise (x) direction (the two-dimensional velocity field is shown in Fig. S2(c)), $u(y) = \langle u(x, y) \rangle_x$, measured in different time periods. The data were taken from a single trap. $t = 0$ is the time at which the trap is filled with cells. Error bars represent the standard error, which we roughly evaluate by picking up 5 data points along the span-wise direction, at intervals of roughly $5 \mu\text{m}$, half of the size of the PIV window. The open end is located near $y \approx 81 \mu\text{m}$. (Inset) The same quantity measured for a PDMS-based device with a similar trap (Fig. S2(a),(b),(c)). The open end is at $y \approx 88 \mu\text{m}$. Time dependence is clearly observed. (d) The growth rate profiles λ , evaluated by $\lambda(y) = \langle \frac{du(x, y)}{dy} \rangle_x$, for the EMPS (main panel) and the PDMS-based device (inset). Error bars represent the standard error of the ensemble.

velocity profile is stable for the EMPS over long time periods, while it gradually decreases for the PDMS-based device (Fig. 2c Main Panel and Inset, respectively). The cell growth rate is then obtained by $\lambda(y) = \langle \frac{du(x, y)}{dy} \rangle_x$, which is shown in Fig. 2d. The result shows that the growth rate λ is indeed uniform and kept constant for the EMPS (Fig. 2(d), Main Panel), while for the PDMS device it is heterogeneous, being higher near the open end (Fig. 2(d), Inset), and it decreases as time elapses. The growth rate decays at the distance of roughly $30 \mu\text{m}$ from the open end, which is located near $y \approx 88 \mu\text{m}$ for the PDMS device. This observation is consistent with the nutrient depletion length we evaluate by following the calculation by Mather et al. [17], $32 \mu\text{m}$, for which we used the diffusion constant of glucose [24] and the division time of 60 min. Such heterogeneity is not seen in the EMPS. While cell growth regulation pathways may also be influenced by such factors as mechanical pres-

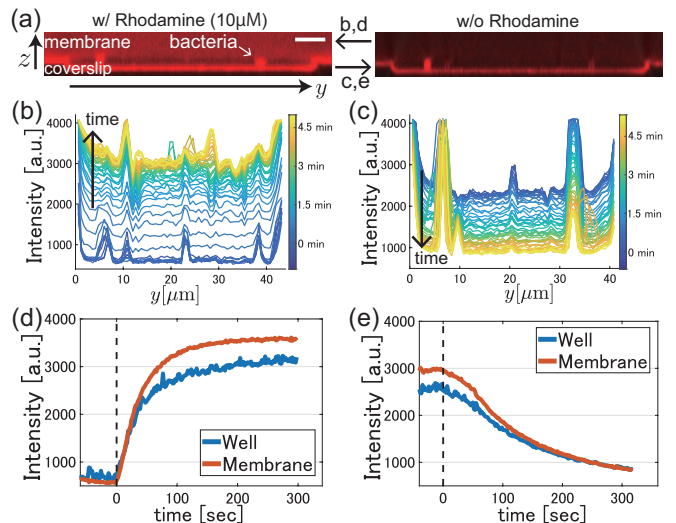


FIG. 3. Direct observations of medium exchange in the EMPS. (a) Cross-sectional images of the device taken by confocal microscopy. The scale bar is $5 \mu\text{m}$. Medium flows from the front side to the rear side of the images. (left) A snapshot of the device filled with a PBS solution with $10 \mu\text{M}$ rhodamine. Bacterial cells and the bilayer membrane are dyed and visualized. (right) A snapshot of the device filled with PBS without rhodamine. The surface of the coverslip and the cells still exhibit fluorescence because of adsorption of rhodamine. (b),(c) Time evolution of the spatial profile of the fluorescent intensity, when the medium is switched to the rhodamine solution ((b), see also Movie S5) and to the PBS without rhodamine ((c), see also Movie S6). The intensity averaged over 5 pixels ($0.6 \mu\text{m}$) from the substrate bottom is shown. The peaks seen in the profiles are due to bacterial cells, walls or dust. (d),(e) Time series of the spatially averaged fluorescence intensity when the medium is switched to the rhodamine solution (d) and to the PBS without rhodamine (e). During the experiment, medium flowed above the membrane at a constant speed of approximately 6 mm/sec . $t = 0$ is the time at which the rhodamine solution entered the device (black dashed line). See Appendix A 7 for details of the experiment and analysis.

sure caused by cell elongation [25–28], quorum sensing [29, 30], etc., our results indicate that the EMPS can indeed realize a uniform and stable culture condition while the same medium is kept supplied.

Another advantage of the EMPS is that we can also switch the culture condition, by changing the medium to supply. Here we evaluate how efficiently the medium in the well is exchanged. In the presence of non-motile *E. coli* W3110 $\Delta\text{fliC} \Delta\text{flu} \Delta\text{fimA}$, we switch the medium to supply from phosphate buffered saline (PBS) to PBS solution of rhodamine fluorescent dye, and monitor the fluorescent signal in a cross-section of the device by a confocal microscope (Fig. 3(a), from right to left). The result shows that the medium inside the well is exchanged uniformly in space (Fig. 3(b)) and that it is almost completed within 2-4 min (Fig. 3(d)). We also change the medium from PBS with rhodamine to that without rho-

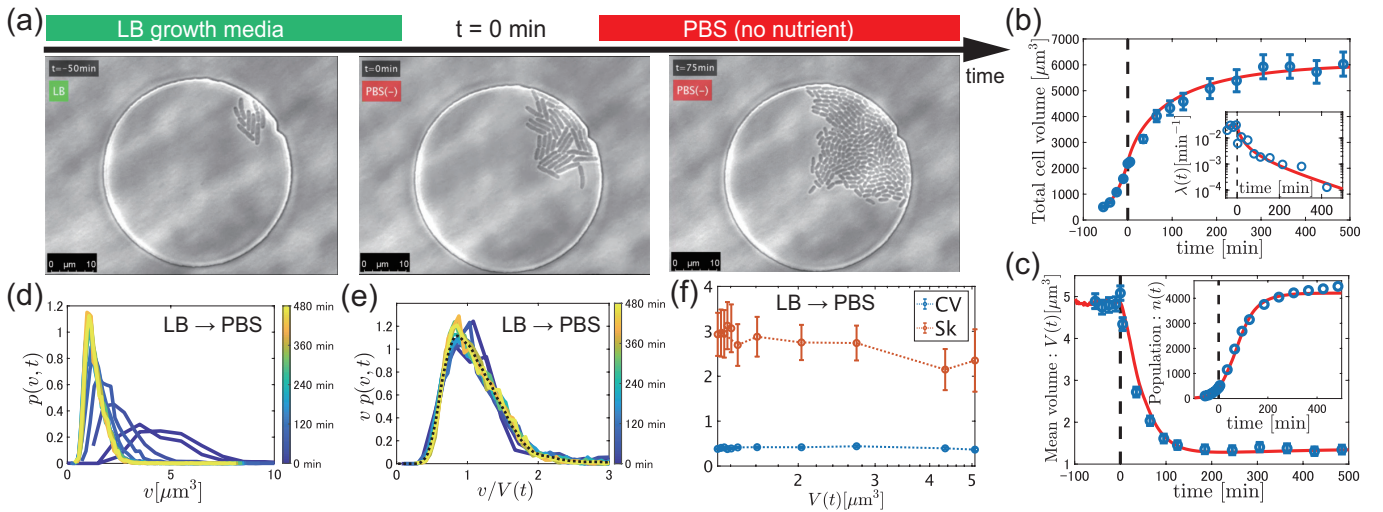


FIG. 4. Results from the observations of reductive division. (a) Snapshots taken during the reductive division process of *E. coli* MG1655 in the EMPS. The medium is switched from LB broth to PBS at $t = 0$. See also Movie S7. (b),(c) Experimental data (blue symbols) for the total cell volume $V_{\text{tot}}(t)$ (b), the growth rate $\lambda(t)$ ((b), Inset), the mean cell volume $V(t)$ (c) and the number of the cells $n(t)$ ((c), Inset) in the case of LB \rightarrow PBS, compared with the simulation results (red curves). The error bars indicate segmentation uncertainty in the image analysis (see Appendix A 8). $t = 0$ is the time at which PBS enters the device (black dashed line). The data were collected from 15 wells. (d) Time evolution of the cell size distributions during starvation in the case of LB \rightarrow PBS at $t = 0, 5, 30, 60, 90, 120, 180, 240, 300, 360, 420, 480$ min from right to left. The sample size is $n(t)$ for each distribution (see (c), Inset). (e) Rescaling of the data in (d). The overlapped curves indicate the function $F(v/V(t))$ in Eq. (2). The dashed line represents the time average of the datasets. (f) CV and Sk [Eq. (3)] against $V(t) = \langle v \rangle$. The error bars were estimated by the bootstrap method with 1000 realizations.

damine (Fig. 3(a), from left to right). The exchange then took longer time, $\gtrsim 5$ min, presumably because of adsorption of rhodamine on the substrate and membrane (see Fig. 3(a)). In any case, the time to take for exchanging medium is much shorter than the timescale of the bacterial cell cycle. Our observations also indicate that the membrane is indeed kept flat above the well (Fig. 3(a)) and that the Brownian motion of non-motile cells is hardly affected by relatively strong medium flow above the membrane (estimated at roughly 6 mm/sec) induced when switching the medium (Movie S5,6). We therefore conclude that the EMPS is indeed able to change the growth condition for cells under observation uniformly, without noticeable fluid flow perturbations.

B. Characterization of bacterial reductive division by EMPS

Now we observe the reductive division of *E. coli* MG1655 in the EMPS, triggering starvation by switching from nutritious medium to non-nutritious buffer. In the beginning, a few cells are trapped in a quasi-two-dimensional well (diameter $55 \mu\text{m}$ and depth $0.8 \mu\text{m}$) and grown in nutritious medium, until a microcolony composed of approximately 100 cells appear. We then quickly switch the medium to a non-nutritious buffer, which is continuously supplied until the end of the observation (see Appendix A 8 for more details). By doing so, we in-

tend to remove various substances secreted by cells, such as autoinducers for quorum sensing and waste products, to reduce their effects on cell growth [29–32]. Throughout this experiment, the well is entirely recorded by phase contrast microscopy. We then measure the length and the width of all cells in the well, to obtain the volume v of each cell by assuming the spherocylindrical shape, at different times before and after the medium switch. Here we mainly show the results for the case where the medium is switched from LB broth to PBS (denoted by LB \rightarrow PBS) in Fig. 4, while the results for M9(Glc+a.a.) \rightarrow PBS, and M9 medium with glucose (Glc) \rightarrow M9 medium with α -methyl-D-glucoside (α MG), a glucose analog which cannot be metabolized [33], are also presented in Fig. S3 and S4. We observe that, after switching to the non-nutritious buffer, the growth of the total volume decelerates (Movie S7-9, Fig. 4(b), Fig. S3(b) and Fig. S4(b)), and the mean cell volume rapidly decays because of excessive cell divisions (Movie S7-9, Fig. 4(a),(c)). The volume change is mostly due to the decrease of the cell length, while we notice that the mean cell width may also change slightly (Fig. S5). We consider that this is not due to osmotic shock [34], because then the cell width would increase when the osmotic pressure is decreased, which is contradictory to our observation for LB \rightarrow PBS (Table S1 and Fig. S5). Such a change in cell widths was also reported for a transition between two different growth conditions [35]. In any case, Fig. 4(d) shows how the distribution of the cell volumes v , $p(v, t)$, changes over

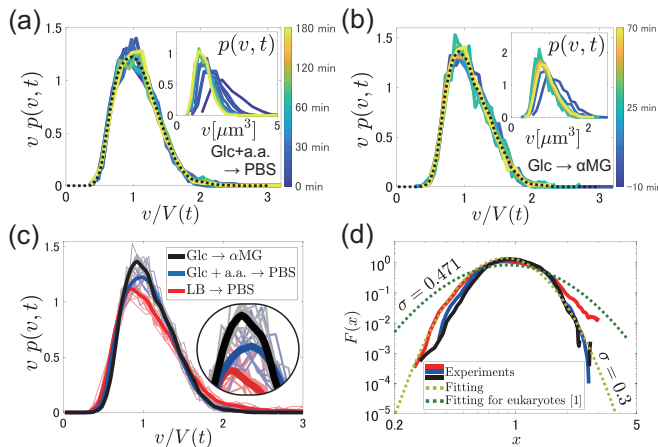


FIG. 5. Rescaled cell size distributions. (a) The results for $M9(\text{Glc}+\text{a.a.}) \rightarrow \text{PBS}$. The dashed line represents the time average of the datasets. The data were taken from 17 wells. The sample size ranges from $n(0) = 685$ to $n(180) = 1260$ (see Fig. S3(c)). (Inset) Time evolution of the non-rescaled cell size distributions at $t = 0, 10, 20, 30, 40, 50, 60, 90, 120, 180$ min. (b) The results for $M9(\text{Glc}) \rightarrow M9(\alpha\text{MG})$. The dashed line represents the time average of the datasets. The data were taken from 26 wells. The sample size ranges from $n(-5) = 1029$ to $n(65) = 1591$ (see Fig. S4(c)). (Inset) Time evolution of the non-rescaled cell size distributions at $t = -5, 5, 10, 20, 25, 30, 35, 50, 65$ min. (c) Experimental results of $F(v/V(t)) = vp(v, t)$ for the three cases studied in this work. The raw data obtained at different times are shown by thin lines with relatively light colors, and the time-averaged data are shown by the bold lines. The time-averaged distributions (bold lines) are found to be slightly but significantly different among the three cases. The difference can also be seen in the instantaneous distributions (thin lines; see the inset for enlargement near the peak). (d) Fitting of the experimentally obtained $F(x)$ (solid lines; time-averaged data in (c) are shown) to the log-normal distribution (yellow dotted line). Also shown is the fitting result by Giometto *et al.* [1] for unicellular eukaryotes (green dotted line). σ is the standard deviation parameter of the log-normal distribution (see text).

time; as the mean volume decreases, the histograms shift leftward and become sharper. However, when we take the ratio $v/V(t)$, with $V(t) = \langle v \rangle$ being the mean cell volume at each time t , and plot $vp(v, t)$ instead, we find that all those histograms overlap onto a single curve (Fig. 4(e)). In other words, we find that the time-dependent cell size distribution during the reductive division maintains the following scale-invariant form all the time:

$$p(v, t) = v^{-1}F(v/V(t)). \quad (2)$$

This is analogous to Eq. (1) previously reported for the steady growth condition, but here importantly the mean volume $V(t)$ changes over time significantly (Fig. 4(c)). To further test the scale invariance of the distribution, we evaluate the coefficient of variation (CV) and the skew-

ness (Sk) defined by

$$\text{CV} \equiv \frac{\sqrt{\langle \delta v^2 \rangle}}{\langle v \rangle}, \quad \text{Sk} \equiv \frac{\langle \delta v^3 \rangle}{\langle \delta v^2 \rangle^{3/2}}, \quad (3)$$

with $\delta v \equiv v - \langle v \rangle$. Both quantities measure the shape of the distribution function of $v/V(t)$ and not affected by variation of $V(t)$. The results in Fig. 4(f) indeed confirm that both CV and Sk remain essentially constant, so that the function $F(\cdot)$ remains unchanged and the scale invariance holds during the reductive division. Remarkably, we reach the same conclusion for all starving conditions that we test, as shown in Fig. 5(a)(b)(c) (see Fig. 4(f), Fig. S3(d) and Fig. S4(d) for the results of CV and Sk) [36]. Our results therefore indicate that the scale invariance as in Eq. (2), which has been observed for steady conditions [1, 2], also holds in non-steady reductive division processes of *E. coli* rather robustly.

In addition to the robustness of the scaling relation (2), the functional form of the scale-invariant distribution, i.e., that of $F(x)$, is of central interest. We detected weak dependence of $F(x)$ on the choice of the medium in the growth phase (Fig. 5(c)). The lower the nutrient level of the growth medium is, the sharper the function $F(x)$ becomes, and therefore, the smaller the variance is. This is somewhat unexpected in view of the past studies reporting the robustness of cell size fluctuations against varying temperatures and other environmental factors [1, 5, 7] [37].

Moreover, we find that our observations for *E. coli* are significantly different from those for unicellular eukaryotes reported by Giometto *et al.* [1] (Fig. 5(d)). More precisely, they showed that the rescaled cell size distribution for unicellular eukaryotes is well fitted by the log-normal distribution, $\propto (1/x) \exp(-(\log x - m)^2/2\sigma^2)$ with $m = -\sigma^2/2$ (due to the normalization $\langle x \rangle = 1$), and obtained $\sigma = 0.471(3)$. We find that our data for *E. coli* can also be fitted by the log-normal distribution (Fig. 5(d), yellow dotted line), but here the value of σ , evaluated by the standard deviation of $\log x$, is found to be around $\sigma = 0.3$ ($\sigma = 0.34(1)$ for $\text{LB} \rightarrow \text{PBS}$, $\sigma = 0.29(2)$ for $M9(\text{Glc}+\text{a.a.}) \rightarrow \text{PBS}$, and $\sigma = 0.28(1)$ for $M9(\text{Glc}) \rightarrow M9(\alpha\text{MG})$), much lower than $\sigma = 0.471(3)$ for the unicellular eukaryotes. In the literature, a previous study on *B. subtilis* [38] reported values of σ from 0.24 to 0.26, which are comparable to our results for *E. coli*. Compared to this substantial difference between bacteria and unicellular eukaryotes, the dependence on the environmental factors seems to be much weaker, as suggested by our observations under three different growth conditions (Fig. 5(d)).

C. Modeling the reductive division process

To obtain theoretical insights on the experimentally observed scale invariance of the cell size distributions, we construct a simple cell cycle model for the bacterial

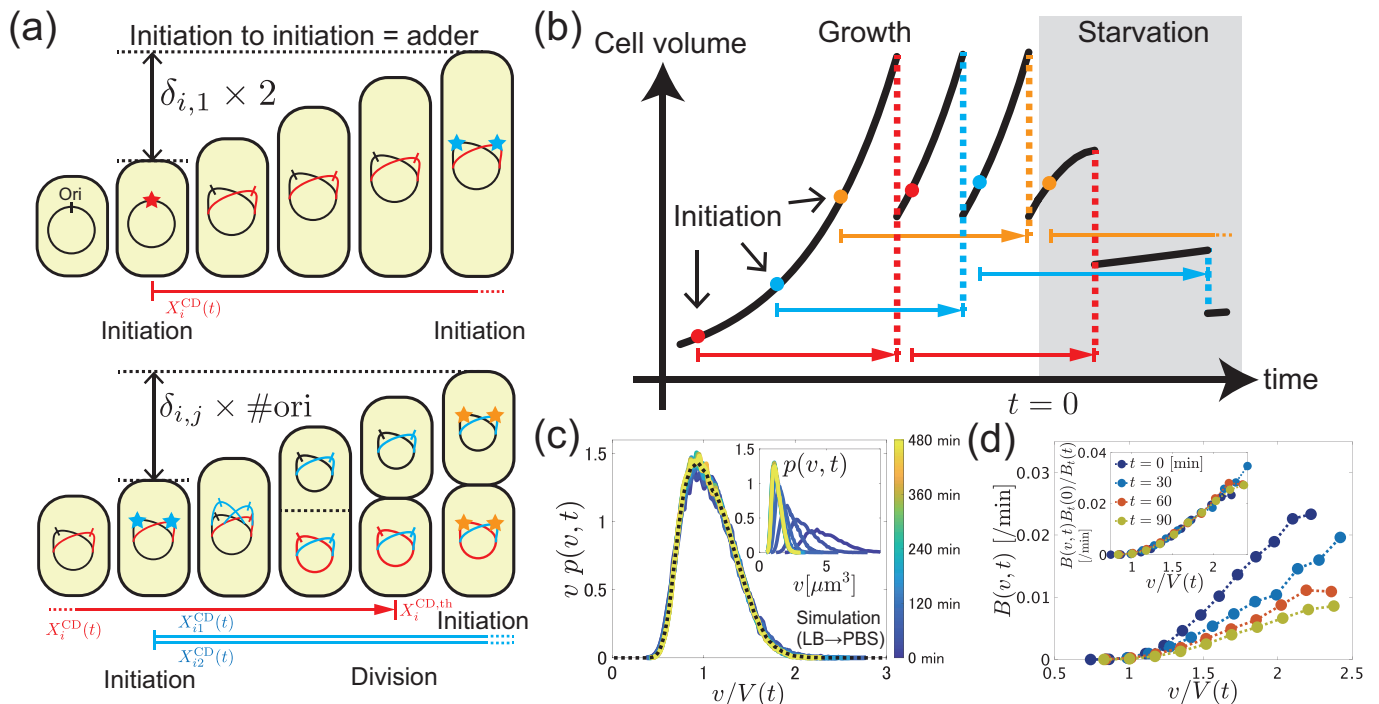


FIG. 6. Model of reductive division and simulation results. (a) Single (top) and multifork (bottom, where $\#\text{ori} = 4$) intracellular cycle processes. See Eq. (4) for the criterion that triggers the initiation. Progress of each cycle is represented by a coordinate $X_i^{\text{CD}}(t)$, which ends at $X_i^{\text{CD}}(t) = X_i^{\text{CD},\text{th}}$ by triggering cell division. In the multifork process, all intracellular cycles proceed simultaneously at the same rate $\mu(t)$. (b) Illustration of cell cycles in this model. Each colored arrow represents a single intracellular cycle process. (c) Overlapping of the rescaled cell size distributions during starvation in the model for LB \rightarrow PBS. The dashed line represents the time average of the datasets. (Inset) The non-rescaled cell size distributions at $t = 0, 5, 30, 60, 90, 120, 180, 240, 300, 360, 420, 480$ min from right to left. (d) Numerically measured division rate, $B(v, t)$, in the model for LB \rightarrow PBS. See Appendix C 2 for the detailed measurement method. (Inset) Test of the condition of Eq. (9). Here $B_t(0)/B_t(t)$ is evaluated by $B_t(0)/B_t(t) = \int B(xV(0), 0)dx / \int B(xV(t), t)dx$, with x running in the range $0 \leq x \leq 1.8$. Overlapping of the data demonstrates that Eq. (9) indeed holds in our model.

reductive division. For the steady growth conditions, a large number of studies on *E. coli* have been carried out to clarify what aspect of cells triggers the division event [8, 9]. Significant advances have been made recently to provide molecular-level understanding [8, 19, 20, 35, 39–42]. Here we extend such a model to describe the starvation process.

One of the most established models in this context is the Cooper-Helmstetter (CH) model [18, 43], which consists of cellular volume growth and multifork DNA replication. The multifork replication is the phenomenon that a cell replicates its DNA not only for its daughters but also for its granddaughters, before the birth of the daughter cells (Fig. 6(a)) – a phenomenon well known for fast growing bacteria such as *E. coli* and *B. subtilis* [18, 43]. In the CH model, completion of the DNA replication triggers the cell division, and this gives a homeostatic balance between the DNA amount and the cell volume. An unknown factor of the CH model is how DNA replication is initiated, and a few studies attempted to fill this gap to complement the CH model [19, 20]. Ho and Amir [19] assumed that replication is initiated when a critical amount of “initiators” accumulate at the origin of repli-

cation. In the presence of a constant concentration of autorepressors, expressed together with the initiators, this assumption means that the cellular volume increases by a fixed amount between two initiation events, regardless of the absolute volume at the initiation. This “adder” principle between initiations is now supported by several observations [40–42]. In contrast, Wallden *et al.* [20] proposed another model based on their experimental observation. In their model, the initiation occurs when the cell volume exceeds a given threshold, independent of the volume added since the last initiation. Clarifying the mechanism of cell division control is currently a target of intensive studies and more refined models have been proposed [40–42]. However, in the present work, we choose to start from the simpler model by Ho and Amir [19], which can already reproduce major characteristics of cell division control in the exponential growth phase, in particular the adder principle between birth and division [9, 44, 45]. We extend Ho and Amir’s model to cope with the switch to the non-nutritious condition, and measure the cell size fluctuations during the reductive division process. We also checked that our main conclusions do not change if we extend Wallden *et al.*’s model instead.

The model consists of two processes that proceed simultaneously, namely the volume growth and the intracellular cycle. The volume of each cell (indexed by i), $v_i(t)$, grows as $\frac{dv_i}{dt} = \lambda(t)v_i(t)$, with a time-dependent growth rate $\lambda(t)$. Following Ho and Amir's CH model [19], we assume that the volume growth is coupled to the intracellular cycle as follows. To begin with the simplest case, suppose that a newborn cell i has a single origin of replication in its chromosome, and that the replication starts at some point in time (Fig. 6(a), top, red star). By this initiation of replication, the cell starts to have two origins of replication. Then, in Ho and Amir's model, the next initiation is triggered when the cell volume $v_i(t)$ increases by a fixed amount $\delta_{i,1}$ per origin, i.e., when $v_i(t)$ increases by $\delta_{i,1} \times 2$, since the last initiation (Fig. 6(a), top, blue stars). Note that this criterion does not change whether a cell divides or not before the initiation; if a cell divides and produces daughter cells i_1 and i_2 , the initiation in the daughter cells occurs when $v_{i_1}(t) + v_{i_2}(t) - v_i(t_{\text{init}}) = \delta_{i,1} \times 2$, where t_{init} is the time at which the last initiation occurred. Similarly, if multifork replication takes place in a single cell (i.e., $\#\text{ori} = 2^j$ with $j \geq 2$), the threshold for the added volume is given by $\delta_{i,j} \times \#\text{ori}$ (see Fig. 6(a), bottom, for an example with $\#\text{ori} = 4$). The criterion therefore reads:

$$\left(\sum_{i' \in \text{offspring of } i} v_{i'}(t) \right) - v_i(t_{\text{init}}) = \delta_{i,j} \times \#\text{ori}. \quad (4)$$

Following the experimental results by Si *et al.* [39], we assume that $\delta_{i,j}$ does not depend on environmental conditions. On the other hand, to take into account stochastic nature of division events, we generate $\delta_{i,j}$ randomly from the Gaussian distribution with mean $\langle \delta_{i,j} \rangle = \delta_{\text{mean}}$ and standard deviation $\text{Std}[\delta_{i,j}] = \delta_{\text{std}}$.

By the initiation considered above, the cell starts the C period of the bacterial cell cycle, which is followed by the D period, and eventually the cell divides [18, 20, 43]. Here, for the sake of simplicity, all these processes are grouped together and expressed as the C+D period. Its progression is represented by a coordinate $X_i^{\text{CD}}(t)$, which starts from zero and increases at time-dependent speed $\mu(t)$, $\frac{dX_i^{\text{CD}}}{dt} = \mu(t)$. When $X_i^{\text{CD}}(t)$ reaches a threshold $X_i^{\text{CD,th}}$, the cell divides (Fig. 6(a), bottom), leaving two daughter cells of volumes $v_{i_1}(t) = x^{\text{sep}}v_i(t)$ and $v_{i_2}(t) = (1 - x^{\text{sep}})v_i(t)$. Here, x^{sep} is randomly drawn from the Gaussian distribution with mean 0.5 (see below and Fig. S6 for its standard deviation). To deal with the multifork replication, the index i of $X_i^{\text{CD}}(t)$ denotes the cell to divide by the considered cell cycle progression. Therefore, if $\#\text{ori} = 2$ when the initiation is triggered, a pair of cell cycles for the future daughter cells, represented by $X_{i_1}^{\text{CD}}(t)$ and $X_{i_2}^{\text{CD}}(t)$, start and run simultaneously (Fig. 6(b)). Similarly to $\delta_{i,j}$, we also assume that $X_i^{\text{CD,th}}$ is a Gaussian random variable, with $\langle X_i^{\text{CD,th}} \rangle = 1$ and $\text{Std}[X_i^{\text{CD,th}}] = X_{\text{std}}^{\text{CD,th}}$.

Now we are left to determine the two time-dependent

rates, $\lambda(t)$ and $\mu(t)$. Here we consider the situation where growth medium is switched to non-nutritious buffer at $t = 0$; therefore, t denotes time passed since the switch to the non-nutritious condition. First, we set the volume growth rate $\lambda(t)$ on the basis of the Monod equation [46], assuming that substrates in each cell are simply diluted by volume growth and consumed at a constant rate, without uptake because of the non-nutritious condition considered here. As a result, we obtain

$$\lambda(t) = \lambda_0 \frac{1 - A}{e^{Ct} - A}, \quad (5)$$

with constant parameters A and C , and the growth rate $\lambda_0 (= \lambda(0))$ in the exponential growth phase (see Appendix B 1 for details). For the cycle progression speed $\mu(t)$, we first note that the C+D period mainly consists of DNA replication, followed by its segregation and the septum formation [43]. Most parts of those processes involve biochemical reactions of substrates, such as deoxynucleotide triphosphates for the DNA synthesis, and assembly of macromolecules such as FtsZ proteins for the septum formation. We therefore assume that the cycle progression speed is determined by the intracellular concentration of relevant substrates and macromolecules, which is known to decrease in the stationary phase [47, 48]. Specifically, we assume that the cycle progression speed is expressed by the Hill equation, $\mu(t) \propto [\text{RM}_{\text{C+D}}]^n / (K^n + [\text{RM}_{\text{C+D}}]^n)$, with $[\text{RM}_{\text{C+D}}]$ being the concentration of the relevant molecules and K, n adjustable parameters. $[\text{RM}_{\text{C+D}}]$ decreases by dilution due to volume growth, degradation, and consumption. Those are assumed not to depend on $\#\text{ori}$, based on the experimental results that the duration of the C+D period is independent of $\#\text{ori}$ in steady environments [39]. Finally, we obtain the following equation for the cycle progression speed:

$$\mu(t) = \mu_0 \frac{k + 1}{k \exp(t/\tau) + 1}, \quad (6)$$

with parameters k and τ , and the cycle progression speed $\mu_0 (= \mu(0))$ in the growth phase (see Appendix B 1).

The parameter values are determined from the experimentally measured total cell volume and the cell number, which our simulations turn out to reproduce very well (Fig. 4(b),(c) and Fig. S3(b),(c)), with the aid of relations reported by Wallden *et al.* [20] for some of the parameters (see Table I for the parameter values used in the simulations, and Appendix B 3 for the estimation method). With the parameters fixed thereby, we measure the cell size fluctuations at different times and find the scale invariance similar to that revealed experimentally (Fig. 6(c) and Fig. S7(b),(d)). The constancy of CV and Sk is also confirmed (Fig. S7(a),(c)). We also evaluate the functional form of the numerically obtained distribution through the fitting to the log-normal distribution, and obtain $\sigma = 0.24(1)$. This value is comparable to the experimental one, though no information on the distribution is used in the parameter adjustment. Interestingly, the scale invariance emerges despite the existence

of characteristic scales in the model definition, such as the typical volume added between initiations, δ_{mean} . To check the robustness of those results, we also extended Wallden *et al.*'s model along the same line and confirmed the scale invariance of similar quality (Fig. S7(e),(f)) (see Appendix B2 for details of the model). These findings suggest the existence of a statistical principle underlying the scale invariance, which is not influenced by details of the model.

D. Theoretical conditions for the scale invariance

To seek for a possible mechanism leading to the scale invariance, here we describe, theoretically, the time dependence of the cell size distribution in a time-dependent process. Suppose $N(v, t)dv$ is the number of the cells whose volume is larger than v and smaller than $v + dv$. If we assume, for simplicity, that a cell of volume v can divide to two cells of volume $v/2$, at probability $B(v, t)$, we obtain the following time evolution equation:

$$\frac{\partial N(v, t)}{\partial t} = -\frac{\partial}{\partial v}[\lambda(t)vN(v, t)] - B(v, t)N(v, t) + 4B(2v, t)N(2v, t). \quad (7)$$

Note that this equation has been studied by numerous past studies for understanding stable distributions in steady conditions [1, 45, 49–53], but here we explicitly include the time dependence of the division rate, $B(v, t)$, for describing the transient dynamics. To clarify a condition for this equation to have a scale-invariant solution, here we assume the scale invariant form, Eq. (2), where $p(v, t) = N(v, t)/n(t)$ and $n(t)$ is the total number of the cells, and obtain the following self-consistent equation (see Appendix C1 for derivation):

$$F(x) = -x \frac{\partial F(x)}{\partial x} - \frac{B(v, t)}{\bar{B}(t)} F(x) + 2 \frac{B(2v, t)}{\bar{B}(t)} F(2x). \quad (8)$$

Here, $x = v/V(t)$ and $\bar{B}(t) = \int dv B(v, t)p(v, t)$. For the scale invariance, Eq. (8) should hold at any time t . This is fulfilled if $B(v, t)$ can be expressed in the following form (see Appendix C1):

$$B(v, t) = B_v(v/V(t))B_t(t). \quad (9)$$

This is a sufficient condition for the cell size distribution to maintain the scale invariant form, Eq. (2), during the reductive division. It is important to remark that, as opposed to Eq. (7), Eq. (8) does not include the growth rate $\lambda(t)$ explicitly. The scale-invariant distribution $F(x)$ is therefore completely characterized by the division rate $B(v, t)$ in this framework.

To test whether the condition of Eq. (9) is satisfied in our model, we measure the division rate $B(v, t)$ in our simulations (Fig. 6(d)). The data overlap if $B(v, t)B_t(0)/B_t(t)$ is plotted against $v/V(t)$, demonstrating that Eq. (9) indeed holds here. In our model,

the cycle progression speed $\mu(t)$ is assumed to be given completely by the concentration of cell cycle-related substrates, which takes the same value for all cells. This may be why the separation of variable, Eq. (9), effectively holds, and the scale invariance follows. On the other hand, our theory does not seem to account for the functional form $F(x)$ of the scale-invariant distribution; the right hand side of Eq. (8) differs significantly from the left hand side, if the numerically obtained $B(v, t)$ is used together with the function $F(x)$ from the simulations or the experiments (Fig. 8 in Appendix). The disagreement did not improve by taking into account the effect of septum fluctuations (see Appendix C3). The lack of quantitative precision is probably not surprising given the simplicity of the theoretical description, which incorporates all effects of intracellular cycles into the simple division rate function $B(v, t)$. The virtue of this theory is that it clarifies that the intracellular cycle seems to have important relevance in the scale invariance and the functional form of the cell size distribution. The significant difference in $F(x)$ identified between bacteria and unicellular eukaryotes (Fig. 5(d)) may be originated from the different replication mechanisms that the two taxonomic domains adopt.

E. Violation of the scale invariance

Here we investigate the robustness of the scale invariance during the reductive division. In particular, we aim to clarify whether it breaks down for other starvation conditions, and if so, what the condition is for the scale invariance to hold. As shown in Fig. 5(c), the form of $F(x)$ obtained by our experiments depends on the growth environment before starvation. This suggests that $F(x)$ may change if one switches between two growth media in a quasistatic manner, i.e., the scale invariance may break down in this case. Motivated by this hypothesis, we numerically investigate whether there is a lower bound on the relaxation speed of the cellular state, below which the scale invariance breaks down. For simplicity, we consider that the environment starts to change at $t = 0$, and the volume growth rate $\lambda(t)$ and the cycle progression speed $\mu(t)$ decrease as follows:

$$\lambda(t) = \lambda(0) \exp(-t/\tau_\lambda), \quad (10)$$

$$\mu(t) = \mu(0) \exp(-t/\tau_\mu). \quad (11)$$

We regard τ_λ , τ_μ and $\lambda(0)$ as free parameters, while $\mu(0)$ is determined from $\lambda(0)$, using empirical relation reported by Wallden *et al.* [20] for steady environments. The number of cells is set to be approximately 50,000 at $t = 0$ and kept constant afterward, by eliminating one of the daughter cells produced by division (see Appendix B3 for details).

First we evaluate the mean cell volume $\langle v \rangle$ and the coefficient of variation, $\text{CV} = \sqrt{\langle \delta v^2 \rangle} / \langle v \rangle$, in the exponential growth phase under steady conditions, by varying the growth rate $\lambda(0)$ from 0.0075 to 0.03 /min. As

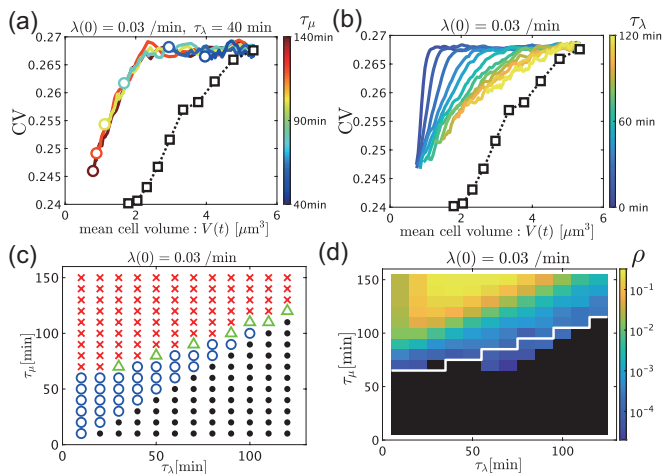


FIG. 7. Numerical results on the range of validity of the scale invariance. The initial growth rate is fixed at $\lambda(0) = 0.03$ /min unless otherwise stipulated. (a) Trajectories in the $\langle v \rangle$ -CV space for different τ_μ (from 50 to 150 min), with $\tau_\lambda = 40$ min fixed. The endpoint of each trajectory is indicated by a colored open circle. The black squares represent the states in steady growth conditions with the growth rate $\lambda(0)$ ranging from 0.0075 to 0.03 /min. (b) The master curves of the $\langle v \rangle$ -CV trajectories for different τ_λ . Those are obtained by taking the average of the CV values at each $\langle v \rangle$ over different $\tau_\mu (> \tau_\lambda)$. τ_λ ranges from 10 to 120 min. (c) Phase diagram. \times : the scale invariance breaks down. Blue o : the scale invariance holds. Green \triangle : near the boundary. Black dots: the scale invariance holds but the mean volume increases. (d) Pseudocolor plot of ρ for different τ_λ and τ_μ . See the main text for the definition of ρ . The black region indicates $\rho = 0$. The white line represents the transition line obtained from (c). The boundaries (\triangle) are included in the region where the scale invariance breaks down.

shown by the black squares in Fig. 7(a)(b), lower growth rates (smaller mean volumes) lead to lower CVs. This is consistent with our experimental results (Fig. 5(c)). We then investigate how the mean volume $\langle v \rangle$ and CV change during the starvation process, starting at $t = 0$ from the growth phase with $\lambda(0) = 0.03$ /min (Fig. 7(a), the top right black square). As expected, our data showed that the mean cell volume decreases if $\tau_\mu > \tau_\lambda$ and increases otherwise; therefore, in the following, we deal with the case of $\tau_\mu > \tau_\lambda$, which corresponds to the reductive division. The color curves in Fig. 7 show trajectories in the $\langle v \rangle$ -CV space during the starvation process, each curve corresponding to a different $\tau_\mu (> \tau_\lambda)$ with τ_λ fixed at $\tau_\lambda = 40$ min. Remarkably, these trajectories overlap to a single curve with an extended plateau region, which indicates that CV is kept constant, i.e., the scale invariance. Each curve stops in the middle of the master curve, the location of the endpoint (at $t \rightarrow \infty$, shown by the open circles) being determined by τ_μ . Importantly, for small τ_μ , the trajectories stop in the plateau region, so that the scale invariance holds during the entire process. By contrast, for large τ_μ , the trajectories go over the plateau and CV decreases abruptly; in other words the scale in-

variance breaks down. Next, Fig. 7(b) shows the master curves for different τ_λ , each constructed by using the trajectories for all τ_μ greater than τ_λ . We find that the smaller τ_λ is, the more extended the plateau region is. Finally, we show the phase diagram for various combinations of τ_μ and τ_λ in Fig. 7(c). This clearly shows a region in which the scale invariance is maintained during the entire starvation process, bordered by a transition line over which the scale invariance breaks down. Note that the scale-invariant region becomes narrower for larger τ_λ and τ_μ and seem to disappear eventually; this is consistent with our expectation described at the beginning, that the scale invariance does not hold for quasistatic changes. All those results are also confirmed for another initial condition, prepared with $\lambda(0) = 0.015$ /min (Fig. S8).

To understand what triggers the violation of the scale invariance, we focus on the state of the multifork replications, since our theory suggested the importance of the division rate, which is controlled by the state of the cell cycle. First, we observe that the change in the number of origins of replication ($\#ori$) during the growth phase is rather stable, doubling (by initiation) and decreasing (by division) between $\#ori = 2^{j-1}$ and 2^j with a fixed j for the majority of cells ($j = 3$ in the case of Fig. 6(b); note that $j - 1$ and j correspond to the numbers of parallel arrows therein). This number is maintained for a while in the starvation process, but eventually it may decrease, because a cell may divide without initiating a new replication during the life. We therefore measure the fraction of such cells, ρ . To be precise, with J being the number of j of the majority of cells in the growth phase, ρ is the fraction of cells such that the C+D period with $j < J$ is initiated during the lifetime, and that this C+D period ends and triggers a cell division afterward, before the cell cycle progression completely stops (note that, since $\mu(t) \rightarrow 0$, not all cell cycles complete). It is measured at the final time point of the simulations (specifically $t = 600$ min). Figure 6(d) shows the results for $\lambda(0) = 0.03$ /min, for which $J = 3$ in the growth phase. Here we find $\rho = 0$ indeed in most part of the scale-invariant region, while $\rho > 0$ when the scale invariance breaks down. We therefore conclude that the state of the multifork replications is indeed a key factor that determines whether the scale invariance holds or not during the reductive division. Note that, for gradual environmental changes, actual cells are known to emit signals such as ppGpp [54, 55] that control growth and cycle progression, which are not taken into account in our model. Investigating the effect of such signals in this problem is an interesting problem left for future studies.

III. CONCLUDING REMARKS

In this work, we developed a novel membrane-based microfluidic device that we named the extensive microprefusion system (EMPS), which can realize a uniformly controlled environment for wide-area observations of mi-

crobes. We believe that the EMPS has potential applications in a wide range of problems with dense cellular populations, including living active matter systems [56, 57] and biofilm growth [58–60]. Here we focused on statistical characterizations of single cell morphology during the reductive division of *E. coli*. Thanks to the EMPS, we recorded the time-dependent distribution of cell size fluctuations and revealed that the rescaled distribution is scale-invariant and robust against the abrupt environmental change, despite the decrease of the mean cell size. This finding was successfully reproduced by simulations of a model based on the CH model [19, 20], which we propose as an extension for dealing with time-dependent environments. We further inspected theoretical mechanism behind this scale invariance and found the significance of the division rate function $B(v, t)$. We obtained a sufficient condition for the scale invariance, Eq. (9), which was indeed confirmed in our numerical data. Finally, we numerically clarified the range of validity of the scale invariance during the reductive division, revealing the crucial role played by the state of the multifork replications. Notably, our experiment (the culture condition dependence, Fig. 5(c)) and simulations (Fig. 7(c)) suggest that the scale invariance breaks down for slow starvation. Further investigations of cell size fluctuations in such cases, both experimentally and theoretically, will be an important step toward clarifying what determines the critical time scale of environmental changes for the violation of the scale invariance.

After all, our theory suggests that mechanism of intracellular replication processes may have direct impact on the scale-invariant distribution, which may account for the significant difference we identified between bacteria and eukaryotes (Fig. 5(d)). Since the number of species studied in each taxonomic domain is rather limited (*E. coli* (this work) and *B. subtilis* [38] for bacteria, 13 protist species for eukaryotes [1]), it is of crucial importance to test the distribution trend further in each taxonomic domain, and to clarify how and to what extent the cell size distribution is determined by the intracellular replication dynamics. Combining with other theoretical methods, such as models considering the cellular age [61], knowledge from the universal protein number fluctuations [62, 63], and renormalization group approaches for living cell tissues [64], may be useful in this context. The influence of cell-to-cell interactions, e.g., quorum sensing [29, 30], may also be important. We hope that our understanding of the population-level response against nutrient starvation will be further refined by future experimental and theoretical investigations.

Appendix A: Experimental Methods

1. Strains and culture media

We used wild-type *E. coli* strains (MG1655 and RP437) and a mutant strain (W3110 Δ fliC Δ flu Δ fimA) in this

study. Culture media and buffer are listed in Table S1. The osmotic pressure of each medium was measured by the freezing-point depression method by the OSMOMAT 030 (Genotec, Berlin Germany). Details on the strains and culture conditions in each experiment are provided below.

2. Fabrication of the PDMS-based device

We prepared PDMS-based microfluidic devices by following the method reported in Ref.[65]. We adopted a microchannel geometry similar to that in Ref.[17], which consists of deep drain channels and shallow U-shape traps (Fig. S2(a),(b)). In our setup, the drain channels are 25 μ m deep, and the U-shape traps are 30 μ m width, 70-90 μ m long, and 1.1 μ m deep. Tygon tubes of 1/16" outer diameter were connected to the inlets and the outlets (Fig. S2(b)) via steel tubes (Elveflow, Paris France). The width of the drains (see Fig. S2(b)) and the length of tygon tubes were adjusted to realize the desired flow rate in the drain near the U-shape traps. The tube length was 55 cm for the medium inlet, 40 cm for the medium outlet, and 30 cm for the waste outlet. The cell inlet was connected to a syringe filled with bacterial suspension via a 10 cm tube, to inject cells at the beginning of observation. After the intrusion of cells, the syringe with the suspension was fixed, and no flow was generated around the cell inlet.

3. Fabrication of the EMPS

The EMPS consists of a microfabricated glass coverslip, a bilayer porous membrane and a PDMS pad. The microfabricated coverslip and the PDMS pad were prepared according to ref. [21, 23]. We fabricated the bilayer porous membrane by combining a streptavidin decorated cellulose membrane and a biotin decorated polyethylene-terephthalate (PET) membrane. The streptavidin decoration of the cellulose membrane (Spectra/Por 7, Repligen, Waltham Massachusetts, molecular weight cut-off 25000) was realized by the method described in ref. [21, 23]. The PET membrane (Transwell 3450, Corning, Corning New York, nominal pore size 0.4 μ m) was decorated with biotin as follows. We soaked a PET membrane in 1 wt% solution of 3-(2-aminoethyl aminopropyl) trimethoxysilane (Shinetsu Kagaku Kogyo, Tokyo Japan) for 45 min, dried it at 125°C for 25 min and washed it by ultrasonic cleaning in Milli-Q water for 5 min. This preprocessed PET membrane was stored in a desiccator at room temperature, until it was used to assemble the EMPS.

The EMPS was assembled as follows. The preprocessed PET membrane was cut into 5 mm \times 5 mm squares, soaked in the biotin solution for 4 hours and dried on filter paper. The biotin decorated PET membrane was attached with a streptavidin decorated cellulose membrane,

cut to the size of the PET membrane, by sandwiching them between agar pads (M9 medium with 2 wt% agarose). In the meantime, a 1 μl droplet of bacterial suspension was inoculated on a biotin decorated coverslip (see also details below). We then took the bilayer membrane from the agar pad, air-dried for tens of seconds, and carefully put on the coverslip on top of the bacterial suspension. The bilayer membrane was then attached to the coverslip via streptavidin-biotin binding as shown in Fig. S1(b). We then air-dried the membrane for a minute and attached a PDMS pad on the coverslip by a double-sided tape.

4. Observation of motile *E. coli* in the EMPS

We used a wild-type motile strain of *E. coli*, RP437. First, we inoculated the strain from a glycerol stock into 2 ml TB medium (see Table S1 for components) in a test tube. After shaking it overnight at 37 °C, we transferred 20 μl of the incubated suspension to 2 ml fresh TB medium and cultured it until the optical density (OD) at 600 nm wavelength reached 0.1-0.5. The bacterial suspension was finally diluted to OD = 0.1 before it was inoculated on the coverslip of the EMPS.

Regarding the device, here we compared the EMPS with the previous system developed in ref. [21], whose membrane was composed of a cellulose membrane alone instead of the bilayer one. In either case, we used a substrate with circular wells of 110-210 μm diameter and 1.1 μm depth. After the assembly of the device with the bacterial suspension, it was fixed on the microscope stage inside an incubation box maintained at 37 °C. The microscope we used was Leica DMI8, equipped with a 63x (N.A. 1.30) oil immersion objective and operated by Leica LasX. To fill the device with medium, we injected fresh TB medium stored at 37 °C from the inlet (Fig. S1), at the rate of 60 ml/hr for 5 min by a syringe pump (NE-1000, New Era Pump Systems, Farmingdale New York).

During the observation, TB medium was constantly supplied from the inlet at the rate of 2 ml/hr (flow speed above the membrane was approximately 0.2 mm/sec) by the syringe pump. Cells were observed by phase contrast microscopy and recorded at the time interval of 30 sec for the cellulose-membrane device (Fig. S1(c)) and 118 msec for the EMPS (Fig. S1(d)). The time interval for the former was long, because cells hardly moved in this case (see Movie S1). We checked that the EMPS can realize quasi-two-dimensional space in which bacteria can freely swim, even for large wells, at least up to 210 μm in diameter, while we have not investigated the reachable largest diameter.

5. Cell growth measurement in U-shape traps in the PDMS-based device

We used a non-motile mutant strain W3110 without flagella and pili ($\Delta\text{fliC } \Delta\text{flu } \Delta\text{fimA}$) to prevent cell adhesion to the surface of a coverslip. Before the time-lapse observation, we inoculated the strain from a glycerol stock into 2 ml M9 medium with glucose and amino acids (Glc+a.a.) (see also Table S1) in a test tube. After shaking it overnight at 37 °C, we transferred 20 μl of the incubated suspension to 2 ml fresh M9(Glc+a.a.) medium and cultured it until the OD at 600 nm wavelength reached 0.4-0.5. We then injected the bacterial suspension into the device from the cell inlet (Fig. S2(b)) and left it until a few cells entered the U-shape traps. The device was placed on the microscope stage, in the incubation box maintained at 37 °C. The microscope we used was Leica DMI8, equipped with a 63x (N.A. 1.30) oil immersion objective and operated by Leica LasX.

During the observation, we constantly supplied M9(Glc+a.a.) medium and 0.5 wt% bovine serum albumin (BSA) from the medium inlet (Fig. S2(b)) at the rate of 0.7 ml/hr (flow speed in the drain was approximately 1 mm/sec). Cells were observed by phase contrast microscopy and recorded at the time interval of 3 min. The velocity field of the coherent flow was obtained by particle image velocimetry, using MatPIV (MATLAB toolbox). The stream-wise component of the velocity field (Fig. 2(c)) was averaged over the span-wise direction, and also over the time period of 150 min.

6. Cell growth measurement in U-shape traps in the EMPS

Here the choice of the strain, the medium, the culture condition and the instruments was the same as those for the measurement with the PDMS-based device, unless otherwise stipulated. Here, the cultured bacterial suspension was diluted to OD = 0.04 before it was inoculated on the coverslip of the EMPS. As sketched in Fig. 2(a), the substrate consisted of drain channels (100 μm wide, 7 mm long, 13 μm deep) and U-shape traps (30 μm wide, 80 μm long, 1.0 μm deep), which were prepared by the methods described in ref. [23]. When the bilayer membrane was attached to the substrate, care was taken not to cover the two ends of the drain channel to use, so that cells in the drain could escape from it. After the assembly of the device with the bacterial suspension, it was fixed on the microscope stage inside the incubation box maintained at 37 °C. To fill the device with medium, we injected fresh medium stored at 37 °C from the inlet (Fig. S1), at the rate of 60 ml/hr for 5 min by a syringe pump (NE-1000, New Era Pump Systems).

During the observation, the flow rate of the M9(Glc+a.a. and BSA) medium was set to be 2 ml/hr (approximately 0.2 mm/sec above the membrane), except that it was increased to 60 ml/hr (approximately

6 mm/sec above the membrane) at a constant interval, in order to remove the cells expelled from the trap efficiently. The time interval of this flush was 60 min before the observed trap was filled with cells, and 30 min thereafter.

7. Evaluation of the rhodamine exchange efficiency in the EMPS

We used a non-motile mutant strain W3110 Δ fliC Δ fliA Δ fimA. Before the time-lapse observation, we inoculated the strain from a glycerol stock into 2 ml M9(Glc+a.a.) medium in a test tube. After shaking it overnight at 37 °C, we transferred 20 μ l of the incubated suspension to 2 ml fresh M9(Glc+a.a.) medium and cultured it until the OD at 600 nm wavelength reached 0.1-0.5. The bacterial suspension was finally diluted to OD = 0.1 before it was inoculated on the coverslip.

Before starting the observations, we injected a PBS solution with 10 μ M rhodamine to adsorb fluorescent dye on the surface of the coverslip, then removed non-adsorbed rhodamine molecules by injecting a pure PBS buffer. We repeated this medium exchange several times. For the observation, we used a laser-scanning confocal microscope, Nikon Ti2, equipped with a 100x (N.A. 1.49) oil immersion objective and operated by Nikon NIS-Elements. The resolution along the Z-axis was 0.12 μ m, and cross-sectional images were taken over a height of 10 μ m, at the time interval of 1.8 sec. In the presence of bacterial cells, we first monitored the fluorescent intensity while we switched the medium to supply from PBS without rhodamine to that containing 10 μ M rhodamine, at the flow rate of 6 mm/sec (approximately 60 ml/hr above the membrane) (Fig. 3(b),(d)). The medium switch was performed by exchanging the syringe connected to the device. After this observation, followed by a time interval of a few minutes without flow of the solution in the device, we started to monitor the fluorescent intensity while we switched the medium from the PBS with rhodamine to that without rhodamine, at the flow rate of 6 mm/sec (Fig. 3(c),(e)).

For evaluating the spatial profile of the fluorescent intensity, the location of the substrate bottom was detected by image analysis in each frame, in order to avoid the influence of vibrations (see Movies S5 and S6) caused by the high flow rate used here. The spatial average of intensity in the well (Fig. 3(d),(e), blue curves) was taken in a square ROI of height 5 pixels (0.6 μ m) from the substrate bottom, and width 200 pixels (24 μ m) along the y-axis, around the center of the well. The spatial average of intensity in the membrane (Fig. 3(d),(e), red curves) was taken in a linear ROI of length 200 pixels (24 μ m) along the y-axis, located at 4.8 μ m above the substrate bottom, around the center.

8. Observation of the bacterial reductive division

We used a wild-type strain MG1655. Before the time-lapse observation, we inoculated the strain from a glycerol stock into 2 ml growth medium in a test tube. The same medium as for the main observation was used (LB broth, M9(Glc+a.a.) or M9(Glc)). After shaking it overnight at 37 °C, we transferred 20 μ l of the incubated suspension to 2 ml fresh medium and cultured it until the OD at 600 nm wavelength reached 0.1-0.5. The bacterial suspension was finally diluted to OD = 0.05 before it was inoculated on the coverslip.

For this experiment, we used a substrate with wells of 55 μ m diameter and 0.8 μ m depth. The well diameter was chosen so that all cells in the well can be recorded. The device was placed on the microscope stage, in the incubation box maintained at 37 °C. The microscope we used was Leica DMi8, equipped with a 100x (N.A. 1.30) oil immersion objective and operated by Leica LasX. To fill the device with growth medium, we injected fresh medium stored at 37 °C from the inlet (Fig. S1), at the rate of 60 ml/hr for 5 min by a syringe pump (NE-1000, New Era Pump Systems).

In the beginning of the observation, growth medium was constantly supplied at the rate of 2 ml/hr (flow speed approximately 0.2 mm/sec above the membrane). When a microcolony composed of approximately 100 cells appeared, we quickly switched the medium to a non-nutritious buffer (PBS or M9 medium with α -methyl-D-glucoside (α MG), see Table S1) stored at 37 °C, by exchanging the syringe. The flow rate was set to be 60 ml/hr for the first 5 minutes, then returned to 2 ml/hr. Throughout the experiment, the device and the media were always in the microscope incubation box, maintained at 37 °C. Cells were observed by phase contrast microscopy and recorded at the time interval of 5 min.

The cell volumes were evaluated as follows. We determined the major axis and the minor axis of each cell, manually, by using a painting software. By measuring the axis lengths, we obtained the set of the lengths L and the widths w for all cells. We then estimated the volume v of each cell, by assuming the spherocylindrical shape of the cell: $v = \frac{4\pi}{3} \left(\frac{w}{2}\right)^3 + \pi \left(\frac{w}{2}\right)^2 (L - w)$. We estimated the uncertainty in manual segmentation at $\pm 0.15 \mu$ m.

Appendix B: Simulations

1. Derivation of Eqs. (5) and (6) for $\lambda(t)$ and $\mu(t)$

Here we describe how we obtained the functional forms of $\lambda(t)$ and $\mu(t)$, Eqs. (5) and (6), in our CH model for the bacterial reductive division (before the simplification described in Sec. II E). We consider the situation where growth medium is switched to non-nutritious buffer at $t = 0$; therefore, t denotes time passed since the switch to the non-nutritious condition. First, on the basis of the

Monod equation [46], we assume that the growth rate $\lambda(t)$ can be expressed as a function of the concentration of substrates, $S(t)$, inside each cell:

$$\lambda(t) = A' \frac{S(t)}{B' + S(t)}, \quad (\text{B1})$$

where A' and B' are constant coefficients. We consider that substrates in each cell are simply diluted by volume growth and consumed at a constant rate C . Therefore,

$$\frac{dS(t)}{dt} = -\lambda(t)S(t) - CS(t). \quad (\text{B2})$$

Note that there is no uptake of substrates because of the non-nutritious condition considered here. By combining Eq. (B1) and Eq. (B2), we obtain the following differential equation for $S(t)$:

$$\frac{dS(t)}{dt} = -\frac{S(t)(A'S(t) + CB' + CS(t))}{B' + S(t)}. \quad (\text{B3})$$

We can solve this equation and obtain

$$S(t) = \frac{DCB'}{e^{Ct} - D(A' + B')}, \quad (\text{B4})$$

where D is a constant of integration. Substituting it to Eq. (B1), we obtain

$$\begin{aligned} \lambda(t) &= \frac{DCA'}{e^{Ct} - D(C - A' - B')} \\ &= \lambda_0 \frac{1 - A}{e^{Ct} - A}, \end{aligned} \quad (\text{B5})$$

with $A = D(C - A' - B')$ and $\lambda_0 = \lambda(0) = DCA'/(1 - D(C - A' - B'))$ being the growth rate in the growth phase, before the onset of starvation.

Next, we determine the functional form of the cycle progression speed $\mu(t)$. We first note that the C+D period mainly consists of DNA replication, followed by its segregation and the septum formation [43]. Most parts of those processes involve biochemical reactions of substrates, such as deoxynucleotide triphosphates for the DNA synthesis, and assembly of macromolecules such as FtsZ proteins for the septum formation. Here, for simplicity, all such molecules are collectively referred to as relevant molecules, represented by $\text{RM}_{\text{C+D}}$, and we simply assume that the progression of the C+D period can be represented by assembly-like processes of relevant molecules. We then consider that the progression speed $\mu(t)$ is given through the Hill equation, which usually describes the binding probability of a receptor and a ligand, with cooperative effect taken into account. Specifically,

$$\mu(t) \propto \frac{[\text{RM}_{\text{C+D}}]^n}{K^n + [\text{RM}_{\text{C+D}}]^n}, \quad (\text{B6})$$

where n is the Hill coefficient, and K is the equilibrium constant of the (collective) assembly process. The

time dependence of the concentration $[\text{RM}_{\text{C+D}}]$ can be evaluated by considering dilution due to volume growth, degradation and consumption:

$$\frac{d[\text{RM}_{\text{C+D}}]}{dt} = -\lambda(t)[\text{RM}_{\text{C+D}}] - E[\text{RM}_{\text{C+D}}], \quad (\text{B7})$$

with a constant rate E . Note that, based on the experimental results that the duration of the C+D period is independent of $\#\text{ori}$ in the steady environments [39], we assumed that $\#\text{ori}$ -dependent consumption is negligible in Eq. (B7). Then, with Eq. (B5), the differential equation becomes

$$\frac{d[\text{RM}_{\text{C+D}}]}{dt} = -\lambda_0 \frac{1 - A}{e^{Ct} - A} [\text{RM}_{\text{C+D}}] - E[\text{RM}_{\text{C+D}}]. \quad (\text{B8})$$

The solution to this equation is

$$[\text{RM}_{\text{C+D}}] = c'_0 \frac{e^{-Ht}}{e^{Ct} - A}, \quad (\text{B9})$$

with a constant c'_0 and $H = E - \lambda_0(1 - A)/A$. To reduce the number of the parameters in the model, we approximate it by an exponential decay, as follows:

$$[\text{RM}_{\text{C+D}}] \approx c_0 \exp(-t/T), \quad (\text{B10})$$

with the initial concentration c_0 and the decay time scale τ . As a result, we obtain

$$\mu(t) = \mu_0 \frac{k + 1}{k \exp(t/\tau) + 1}, \quad (\text{B11})$$

with $k = (K/c_0)^n$, $\tau = T/n$, and $\mu_0 (= \mu(0))$ being the cycle progression speed in the growth phase before the onset of starvation.

2. Extension of the model by Wallden *et al.*

Wallden *et al.*'s CH model [20] assumed that the first DNA replication starts when the cell volume $v_i(t)$ exceeds a fixed threshold $v_{i,1}^{\text{th}}$. Similarly, at $v_i(t) = v_{i,j}^{\text{th}}$, the j th replication (with $\#\text{ori} = 2^j$) is triggered. Following Refs.[20, 39], we assume that the initiation volume $v_{i,j}^{\text{th}}$ takes a constant value per $\#\text{ori}$ for any environmental conditions, so that typically $v_{i,j}^{\text{th}} \approx 2^{j-1}v_{i,1}^{\text{th}}$. To take into account stochastic nature of division events, $v_{i,j}^{\text{th}}$ is generated randomly from the Gaussian distribution with mean $\langle v_{i,j}^{\text{th}} \rangle = 2^{j-1}v_{\text{mean}}^{\text{th}}$ and standard deviation $\text{Std}[v_{i,j}^{\text{th}}] = 2^{j-1}v_{\text{std}}^{\text{th}}$. The standard deviation $v_{\text{std}}^{\text{th}}$ was set to be 10% of the mean $v_{\text{mean}}^{\text{th}}$, based on the relation found by Wallden *et al.* [20]. The other parts of the model are identical to those of the model based on Ho and Amir's one [19].

3. Simulation methods

The parameters used in the simulations were evaluated as follows. First, from the observations of the exponential

TABLE I. Parameters used for the simulations.

Parameters	Parameters	Base: Ho and Amir [19]		Base: Wallden <i>et al.</i> [20]
		LB→PBS	M9(Glc+a.a.)→PBS	LB→PBS
Parameters on the exponential growth phase	$\lambda(0) = \lambda_0$ $\mu(0)^{-1} = \mu_0^{-1}$ δ_{mean} or $v_{\text{mean}}^{\text{th}}$ δ_{std} or $v_{\text{std}}^{\text{th}}$ $X_{\text{std}}^{\text{CD,th}}$ $x_{\text{std}}^{\text{sep}}$	0.029 /min $1.3\lambda_0^{-0.84} + 42 \simeq 67$ min $\delta_{\text{mean}} = 0.25 \mu\text{m}^3$ $0.1 \times \delta_{\text{mean}} = 0.025 \mu\text{m}^3$ $0.05 \times \langle X_i^{\text{CD,th}} \rangle = 0.05$ 0.0325	0.010 /min $1.3\lambda_0^{-0.84} + 42 \simeq 104$ min $\delta_{\text{mean}} = 0.225 \mu\text{m}^3$ $0.1 \times \delta_{\text{mean}} = 0.0225 \mu\text{m}^3$ $0.05 \times \langle X_i^{\text{CD,th}} \rangle = 0.05$ 0.0325	0.029 /min $1.3\lambda_0^{-0.84} + 42 \simeq 67$ min $v_{\text{mean}}^{\text{th}} = 1.0 \mu\text{m}^3$ $0.1 \times v_{\text{mean}}^{\text{th}} = 0.1 \mu\text{m}^3$ $0.05 \times \langle X_i^{\text{CD,th}} \rangle = 0.05$ 0.0325
Time-dependent rates	$\lambda(t) = \lambda_0 \frac{1-A}{e^{Ct}-A}$ $\mu(t) = \mu_0 \frac{k+1}{ke^{t/\tau}+1}$	$A = 0.93, C = 0.0059$ /min $k = 1, \tau = 60$ min	$A = 0.84, C = 0.011$ /min $k = 0.1, \tau = 24$ min	$A = 0.93, C = 0.0059$ /min $k = 10, \tau = 75$ min

growth phase, we determined the growth rate λ_0 directly. This allowed us to set the cycle progression speed μ_0 too, by using the relation $\mu_0^{-1} \simeq (1.3\lambda_0^{-0.84} + 42)$ proposed by Wallden *et al.* [20] (the values of λ_0 and μ_0 in the unit of min^{-1} are used here). Concerning the volume threshold for initiating the replication, we found such a value of δ_{mean} (or $v_{\text{mean}}^{\text{th}}$) that reproduced the experimentally observed mean cell volume in the growth phase. The standard deviation δ_{std} (or $v_{\text{std}}^{\text{th}}$) was set to be 10% of the mean δ_{mean} ($v_{\text{mean}}^{\text{th}}$), based on the relation on the initiation volume found by Wallden *et al.* [20]. They also measured the fluctuations of the time length of the C+D period; this led us to estimate $X_{\text{std}}^{\text{CD,th}}$ at 5% of $\langle X^{\text{CD,th}} \rangle$, i.e., $X_{\text{std}}^{\text{CD,th}} = 0.05$. On the septum positions, we measured their fluctuations and found little difference in $x_{\text{std}}^{\text{sep}}$ among the different growth conditions we used, and also in the non-nutritious case (Fig. S6). We therefore used a single value $x_{\text{std}}^{\text{sep}} = 0.0325$ for all simulations.

In the following, we describe how the remaining parameters were evaluated and how the simulations were carried out for each set of the simulations presented in this work.

a. Methods for the results that reproduced the experimental observations (Sec. IIC)

We evaluated the time-dependent rates $\lambda(t)$ and $\mu(t)$ as follows. The growth rate $\lambda(t)$ can be determined independently of the cell divisions, because the total volume $V_{\text{tot}}(t) = \sum_i v_i(t)$ grows as $V_{\text{tot}}(t) = V_{\text{tot}}(0) \exp(\int_0^t \lambda(t) dt)$. With $\lambda(t)$ given by Eq. (5), we compared $V_{\text{tot}}(t)$ with experimental data and determined the values of A and C (Fig. 5(c)). Finally, only k and τ in Eq. (6) remained as free parameters. We tuned them so that the mean cell volume $V(t)$ and the number of the cells $n(t)$ observed in the simulations reproduced those from the experiments (Fig. 5(d)).

The parameter values determined thereby are summarized in Table I, for the simulations for LS→PBS and M9(Glc+a.a.)→PBS. Note that we did not perform simulations for M9(Glc)→M9(α MG), because we found it difficult to fit the experimental data for $V_{\text{tot}}(t)$ and $n(t)$

in this case (Fig. S4). This suggests that the consequence of the replacement of glucose by glucose analog α MG may not be simple starvation.

We started the simulations from 10 cells with volumes in the range of 0.07-1.13 μm^3 , randomly generated from the uniform distribution. The cells grew in the exponential phase (with the constant growth rate λ_0 and the cycle progression speed μ_0) until the number of cells reached 100,000. We then randomly picked up 10 cells from this ‘‘precultured’’ sample and grew them until the number of cells exceeded 500. Those cells were kept growing for 1000 minutes to sufficiently mix cell cycle progressions in the population. During this process, we kept the number of cells constant, by eliminating one of the daughter cells after each division. We then used them as the initial population of each simulation. To precisely compare the number of cells in simulations with the experimentally obtained population $n_{\text{exp}}(t)$ (Fig. 4(c) and Fig. S3(c)), the numerically obtained population $n_{\text{sim}}(t)$ is rescaled by multiplying $n_{\text{exp}}(0)/n_{\text{sim}}(0)$.

b. Methods for the results on violation of the scale invariance (Sec. IIE)

The functional forms of $\lambda(t)$ and $\mu(t)$ were given by Eqs. (10) and (11), with variable parameters τ_λ and τ_μ . The other parameters were fixed at $\delta_{\text{mean}} = 0.25 \mu\text{m}^3$, $\delta_{\text{std}} = 0.025 \mu\text{m}^3$, $X_{\text{std}}^{\text{CD,th}} = 0.05$, and $x_{\text{std}}^{\text{sep}} = 0.0325$. We started the simulations from 50 cells with volumes in the range of 0.07-1.13 μm^3 , randomly generated from the uniform distribution. The cells grew in the exponential phase until the number of cells reached 500,000. We then randomly picked up 50 cells and grew them until the number of cells exceeded 50,000. Those cells were kept growing for 1,000 minutes to sufficiently mix cell cycle progressions in the population, with the number of cells kept constant by eliminating one of the daughter cells produced by division. Using them as the initial population (at $t = 0$), we started the simulations for $t \geq 0$, with the number of cells still kept constant by the same method.

Appendix C: Theory

1. Theoretical conditions for the scale invariance

Here, we describe the detailed derivation of the sufficient condition for the scale invariance of the cell size distribution. We start from the time evolution equation, Eq. (7):

$$\begin{aligned} & \frac{\partial N(v, t)}{\partial t} \\ &= -\frac{\partial}{\partial v} [\lambda(t)vN(v, t)] - B(v, t)N(v, t) + 4B(2v, t)N(2v, t), \end{aligned} \quad (\text{C1})$$

where $\lambda(t)$ is the growth rate and $B(v, t)$ is the division rate function (see the main article for its definition). We assume the scale invariance in the form of Eq. (2) for the cell size distribution $p(v, t) = N(v, t)/n(t)$, where $n(t) = \int_0^\infty N(v, t)dv$ is the total number of the cells. For $N(v, t)$, this reads

$$N(v, t) = \frac{n(t)}{v} F\left(\frac{v}{V(t)}\right), \quad (\text{C2})$$

where $V(t)$ is the mean cell volume at time t , $V(t) = \langle v \rangle$. One can then rewrite the time evolution equation (C1) in terms of the function $F(x)$ with $x = v/V(t)$, as follows:

$$\begin{aligned} & \frac{\partial n(t)}{\partial t} \frac{1}{v} F(x) - \frac{n(t)}{V(t)^2} \frac{\partial V(t)}{\partial t} \frac{\partial F(x)}{\partial x} \\ &= -\lambda(t)n(t) \frac{1}{V(t)} \frac{\partial F(x)}{\partial x} \\ & \quad - B(v, t) \frac{n(t)}{v} F(x) + 4B(2v, t) \frac{n(t)}{2v} F(2x). \end{aligned} \quad (\text{C3})$$

If we neglect cell-to-cell fluctuations of the growth rate, one can evaluate $\lambda(t)$ from the total biomass growth, as follows:

$$\begin{aligned} \lambda(t) &= \frac{d(V(t)n(t))}{dt} (V(t)n(t))^{-1} \\ &= \left(V(t) \frac{\partial n(t)}{\partial t} + n(t) \frac{\partial V(t)}{\partial t} \right) (n(t)V(t))^{-1} \\ &= \frac{1}{n(t)} \frac{\partial n(t)}{\partial t} + \frac{1}{V(t)} \frac{\partial V(t)}{\partial t}. \end{aligned} \quad (\text{C4})$$

From Eqs. (C3) and (C4), we obtain

$$\begin{aligned} & \frac{\partial n(t)}{\partial t} \frac{1}{v} F(x) = -\frac{1}{V(t)} \frac{\partial n(t)}{\partial t} \frac{\partial F(x)}{\partial x} \\ & \quad - \frac{B(v, t)}{v} n(t) F(x) + 4 \frac{B(2v, t)}{2v} n(t) F(2x). \end{aligned} \quad (\text{C5})$$

Now, the time derivative of $n(t)$ can be calculated as

$$\begin{aligned} \frac{\partial n(t)}{\partial t} &= \int_0^\infty dv \frac{\partial N(v, t)}{\partial t} \\ &= -\int_0^\infty dv B(v, t) N(v, t) \\ & \quad + 4 \int_0^\infty dv' B(2v', t) N(2v', t) \\ &= n(t) \int_0^\infty dv \frac{B(v, t)}{v} F\left(\frac{v}{V(t)}\right) \\ &= n(t) \bar{B}(t), \end{aligned} \quad (\text{C6})$$

where $\bar{B}(t) = \int_0^\infty dv B(v, t) p(v, t) = \int_0^\infty dv B(v, t) v^{-1} F(v/V(t))$. Substituting it to Eq. (C5), we finally obtain the following self-consistent equation for $F(x)$ (Eq. (8)):

$$F(x) = -x \frac{\partial F(x)}{\partial x} - \frac{B(v, t)}{\bar{B}(t)} F(x) + 2 \frac{B(2v, t)}{\bar{B}(t)} F(2x). \quad (\text{C7})$$

For the scale invariance, Eq. (C7) should hold at any time t . In other words, the coefficient $B(v, t)/\bar{B}(t)$ should be independent of both t and $V(t)$. Note here that $B(v, t)/\bar{B}(t)$ can be rewritten as

$$\begin{aligned} \frac{\bar{B}(t)}{B(v, t)} &= \int_0^\infty dv' \frac{B(v', t)}{B(v, t)} \frac{1}{v'} F\left(\frac{v'}{V(t)}\right) \\ &= \int_0^\infty dx' \frac{B(x'V(t), t)}{B(xV(t), t)} \frac{1}{x'} F(x'). \end{aligned} \quad (\text{C8})$$

Therefore, $B(v, t)/\bar{B}(t)$ is time-independent if $\frac{B(x'V(t), t)}{B(xV(t), t)}$ does not depend on $V(t)$, being a function of two dimensionless variables x and x' only, as follows:

$$\frac{B(x'V(t), t)}{B(xV(t), t)} = \beta(x', x). \quad (\text{C9})$$

This condition can be rewritten as follows. For a constant x_0 , we can define $B_t(t)$ by

$$B(x_0V(t), t) = B_t(t) \quad (\text{C10})$$

and $B_v(x)$ by

$$\beta(x, x_0) = B_v(x). \quad (\text{C11})$$

Then, the division rate can be expressed as $B(xV(t), t) = B_v(x)B_t(t)$ for any x and t . This gives the sufficient condition we presented in the main text, Eq. (9),

$$B(v, t) = B_v\left(\frac{v}{V(t)}\right) B_t(t). \quad (\text{C12})$$

2. Test of the derived conditions for $B(v, t)$ and $F(x)$

We tested the sufficient condition for $B(v, t)$ (Eq. (C12)) and the resulting self-consistent equation for $F(x)$ (Eq. (C7)) with numerical data we obtained from our CH model (Fig. 5(d)). We evaluated the division rate $B(v, t)$ in the simulations for LB \rightarrow PBS by

$$B(v, t) = \frac{\# \text{ of division events of cells of volume between } v \text{ and } v + \Delta v, \text{ between time } t \text{ and } t + \Delta t}{\# \text{ of cells of volume between } v \text{ and } v + \Delta v \text{ at time } t}. \quad (\text{C13})$$

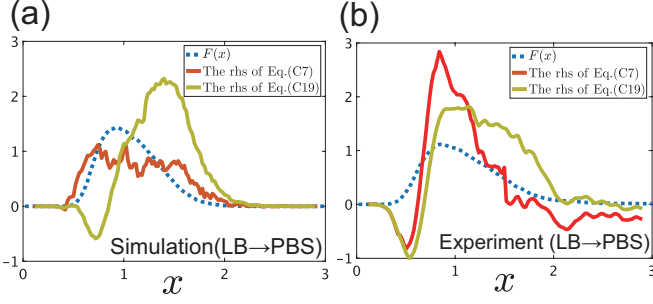


FIG. 8. Test of the self-consistent equations derived in Supplementary Theory. The functional form of $F(x)$, obtained numerically (a) or experimentally (b) for the case $\text{LB} \rightarrow \text{PBS}$, is compared with the right-hand side (rhs) of the self-consistent equations derived in Supplementary Theory, Eqs. (C7) and (C19). The effect of septum fluctuations is neglected in Eq. (C7) and considered in Eq. (C19). $F(x)$ is obtained as the time average of the instantaneous data.

Here, Δv was set to be approximately $0.2 \times V(t)$ and Δt to be approximately 20-30 min for each time point, respectively. The value of $B(v, 0)$ was determined by counting all division events in the exponential growth phase ($t < 0$). The ratio $B_t(0)/B_t(t)$ can be evaluated by $B_t(0)/B_t(t) = \int B(xV(0), 0)dx / \int B(xV(t), t)dx$. We found that the curves $B(v, t)B_t(0)/B_t(t)$ taken at different t overlap reasonably well (Fig. 5(d), Inset), which support the variable separability condition of the division rate, Eq. (C12).

Given the functional form of $B(v, t)$ that we obtained numerically, we can also test the self-consistent equation for $F(x)$, Eq. (C7). Here we remind that the ratio $B(v, t)/\bar{B}(t)$ in Eq. (C7) can be expressed as Eq. (C8), and $\frac{B(x'V(t), t)}{B(xV(t), t)}$ is time-independent (cf. Eq. (C9)). Therefore,

$$\frac{\bar{B}(t)}{B(v, t)} = \int_0^\infty dx' \frac{B(x'V(0), 0)}{B(xV(0), 0)} \frac{1}{x'} F(x') \quad (\text{C14})$$

with $B(xV(0), 0) = B(v, 0) = B(v, t)B_t(0)/B_t(t)$. Since we already confirmed the time independence of $B(v, t)B_t(0)/B_t(t)$ (Fig. 5(d), Inset), we took the average of this quantity obtained at $t = 0, 30, 60, 90$ min. Since

the observed range of v is finite and $F(x)$ almost vanishes for $x \gtrsim 2$, we evaluated the integral over x' in the range $0 \leq x' \leq 2$.

With the $\bar{B}(t)/B(v, t)$ evaluated thereby, we substituted $F(x)$ obtained by the simulations for $\text{LB} \rightarrow \text{PBS}$ to Eq. (C7) (Fig. 8(a)), using the time average of $F(x)$ (the dashed line in Fig. 5(c)) and $F(x) = 0$ for $x \geq 2$. We also tested Eq. (C7) with $F(x)$ obtained in the experiment for $\text{LB} \rightarrow \text{PBS}$, in the same way as for the model (Fig. 8(b)). In both cases, the right-hand side (rhs) of Eq. (C7) differs significantly from the observed form of $F(x)$.

3. Theory with septum fluctuations

As a possible improvement of our theory, here we take into account septum fluctuations. We define the kernel function $q(v|\nu)$ which represents the probability that a mother cell of volume ν produces daughter cells of volume v and $\nu - v$ (therefore, $q(v|\nu) = q(\nu - v|\nu)$). The time evolution equation of $N(v, t)$ is then written as

$$\frac{\partial N(v, t)}{\partial t} = - \frac{\partial(\lambda(t)vN(v, t))}{\partial v} - B(v, t)N(v, t) + \int_v^\infty q(v|\nu)B(\nu, t)N(\nu, t) \frac{\nu}{v} d\nu. \quad (\text{C15})$$

Now, assuming that the fluctuations of the septum position are Gaussian for simplicity, we have

$$q(v|\nu) = 2 \times \sqrt{\frac{1}{2\pi(\xi\nu)^2}} \exp\left(-\frac{(v - \nu/2)^2}{2(\xi\nu)^2}\right), \quad (\text{C16})$$

where the coefficient 2 corresponds to the two daughter cells produced from a single division event. Here, following experimental observations (Fig. S6, see also [45]), we assumed that the standard deviation is proportional to the volume of the mother cell, ν , with coefficient $\xi = 0.0325$.

Under this modification, we obtain the self-consistent equation for $F(x)$ as follows. One can again calculate the time derivative of $n(t)$ as

$$\begin{aligned} \frac{\partial n(t)}{\partial t} &= \int_0^\infty dv \frac{\partial N(v, t)}{\partial t} \\ &= -n(t) \int_0^\infty dv B(v, t)p(v, t) + n(t) \sqrt{\frac{2}{\pi\xi^2}} \int_0^\infty dv' \int_{v'}^\infty dv \frac{B(\nu, t)}{v'} p(\nu, t) \exp\left(-\frac{(v'/\nu - 1/2)^2}{2\xi^2}\right) \\ &= n(t)\bar{B}_2(t), \end{aligned} \quad (\text{C17})$$

where $\overline{B_2}(t)$ is defined by

$$\overline{B_2}(t) = - \int_0^\infty dv B(v, t) p(v, t) + \sqrt{\frac{2}{\pi \xi^2}} \int_0^\infty dv' \int_{v'}^\infty dv \frac{B(v, t)}{v'} p(v, t) \exp\left(-\frac{(v'/\nu - 1/2)^2}{2\xi^2}\right). \quad (\text{C18})$$

With $x = v/V(t)$ and $y = \nu/V(t)$, one can obtain the self-consistent equation for $F(x)$ as

$$F(x) = -x \frac{\partial F(x)}{\partial x} - \frac{B(V(t)x, t)}{\overline{B_2}(t)} F(x) + \sqrt{\frac{2}{\pi \xi^2}} \int_x^\infty dy \frac{B(V(t)y, t)}{\overline{B_2}(t)} y^{-1} \exp\left(-\frac{(x/y - 1/2)^2}{2\xi^2}\right) F(y). \quad (\text{C19})$$

with

$$\frac{\overline{B_2}(t)}{B(V(t)x, t)} = \int_0^\infty dx' \left(-\frac{B_v(x')}{B_v(x)} \frac{F(x')}{x'} + \sqrt{\frac{2}{\pi \xi^2}} \frac{1}{x'} \int_{x'}^\infty dy' \frac{B_v(y')}{B_v(x)} \exp\left(-\frac{(x'/y' - 1/2)^2}{2\xi^2}\right) \frac{F(y')}{y'} \right), \quad (\text{C20})$$

$$\frac{\overline{B_2}(t)}{B(V(t)y, t)} = \int_0^\infty dx' \left(-\frac{B_v(x')}{B_v(y)} \frac{F(x')}{x'} + \sqrt{\frac{2}{\pi \xi^2}} \frac{1}{x'} \int_{x'}^\infty dy' \frac{B_v(y')}{B_v(y)} \exp\left(-\frac{(x'/y' - 1/2)^2}{2\xi^2}\right) \frac{F(y')}{y'} \right). \quad (\text{C21})$$

We tested this for both experimentally and numerically observed $F(x)$, but the modification did not improve the results (Fig. 8).

ACKNOWLEDGMENTS

We are grateful to Y. Himeoka for motivating us to compare the abrupt and quasi-static changes, which led

to the results presented in Fig. 7. We also acknowledge useful discussions with H. Chaté, Y. Furuta, T. Hiraiwa, Y. Kitahara, H. Nakaoka, and D. Nishiguchi. We thank I. Naguro for letting us use the OSMOMAT 030. This work is supported by KAKENHI from Japan Society for the Promotion of Science (JSPS) (No. 16H04033, No. 19H05800), a Grant-in-Aid for JSPS Fellows (No. 20J10682) and by the grants associated with the ‘‘Planting Seeds for Research’’ program and Suematsu Award from Tokyo Tech.

-
- [1] A. Giometto, F. Altermatt, F. Carrara, A. Maritan, and A. Rinaldo, ‘‘Scaling body size fluctuations,’’ *Proc. Natl. Acad. Sci. USA* **110**, 4646–4650 (2013).
 - [2] S. Zaoli, A. Giometto, E. Marañón, S. Escrig, A. Meibom, A. Ahluwalia, R. Stocker, A. Maritan, and A. Rinaldo, ‘‘Generalized size scaling of metabolic rates based on single-cell measurements with freshwater phytoplankton,’’ *Proc. Natl. Acad. Sci. USA* **116**, 17323–17329 (2019).
 - [3] J. Camacho and R. V. Solé, ‘‘Scaling in ecological size spectra,’’ *EPL* **55**, 774–780 (2001).
 - [4] P. A. Marquet, R. A. Quiñones, S. Abades, F. Labra, M. Tognelli, M. Arim, and M. Rivadeneira, ‘‘Scaling and power-laws in ecological systems,’’ *J. Exp. Biol.* **208**, 1749–1769 (2005).
 - [5] S. Iyer-Biswas, C. S. Wright, J. T. Henry, K. Lo, S. Burov, Y. Lin, G. E. Crooks, S. Crosson, A. R. Dinner, and N. F. Scherer, ‘‘Scaling laws governing stochastic growth and division of single bacterial cells,’’ *Proc. Natl. Acad. Sci. USA* **111**, 15912–15917 (2014).
 - [6] A. S. Kennard, M. Osella, A. Javer, J. Grilli, P. Nghe, S. J. Tans, P. Cicuta, and M. Cosentino Lagomarsino, ‘‘Individuality and universality in the growth-division laws of single *E. coli* cells,’’ *Phys. Rev. E* **93**, 012408 (2016).
 - [7] S. Iyer-Biswas, G. E. Crooks, N. F. Scherer, and A. R. Dinner, ‘‘Universality in stochastic exponential growth,’’ *Phys. Rev. Lett.* **113**, 028101 (2014).
 - [8] P. Ho, J. Lin, and A. Amir, ‘‘Modeling cell size regulation: From single-cell-level statistics to molecular mechanisms and population-level effects,’’ *Annu. Rev. Biophys.* **47**, 251–271 (2018).
 - [9] S. Jun, F. Si, R. Pugatch, and M. Scott, ‘‘Fundamental principles in bacterial physiology/history, recent progress, and the future with focus on cell size control: a review,’’ *Rep. Prog. Phys.* **81**, 056601 (2018).
 - [10] C. Cadart, L. Venkova, P. Recho, M. C. Lagomarsino, and M. Piel, ‘‘The physics of cell-size regulation across timescales,’’ *Nat. Phys.* **15**, 993–1004 (2019).
 - [11] T. Nyström, ‘‘Stationary-phase physiology,’’ *Annu. Rev. Microbiol.* **58**, 161–181 (2004).
 - [12] A. S. Kaprelyants and D. B. Kell, ‘‘Dormancy in stationary-phase cultures of *micrococcus luteus*: Flow cytometric analysis of starvation and resuscitation,’’ *Appl. Environ. Microbiol.* **59**, 3187–3196 (1993).
 - [13] C. R. Arias, S. LaFrentz, W. Cai, and O. Olivares-Fuster, ‘‘Adaptive response to starvation in the fish pathogen *Flavobacterium columnare*: cell viability and ultrastructural changes,’’ *BMC Microbiol.* **12** (2012), 10.1186/1471-2180-12-266.
 - [14] D. A. Gray, G. Dugar, P. Gamba, H. Strahl, M. J. Jonker, and L. W. Hamoen, ‘‘Extreme slow growth as alternative strategy to survive deep starvation in bacteria,’’ *Nat. Commun.* **10** (2019), 10.1038/s41467-019-08719-8.

- [15] P. Wang, L. Robert, J. Pelletier, W. L. Dang, F. Taddei, A. Wright, and S. Jun, “Robust growth of *Escherichia coli*,” *Curr. Biol.* **20**, 1099–1103 (2010).
- [16] H. Cho, H. Jönsson, K. Campbell, P. Melke, J. W. Williams, B. Jedynak, A. M. Stevens, A. Groisman, and A. Levchenko, “Self-organization in high-density bacterial colonies: Efficient crowd control,” *PLoS Biol.* **5**, e302 (2007).
- [17] W. Mather, O. Mondragón-Palomino, T. Danino, J. Hasty, and L. S. Tsimring, “Streaming instability in growing cell populations,” *Phys. Rev. Lett.* **104**, 208101 (2010).
- [18] S. Cooper and C. E. Helmstetter, “Chromosome replication and the division cycle of *Escherichia coli* Br,” *J. Mol. Biol.* **31**, 519 – 540 (1968).
- [19] P. Ho and A. Amir, “Simultaneous regulation of cell size and chromosome replication in bacteria,” *Front. Microbiol.* **6**, 662 (2015).
- [20] M. Wallden, D. Fange, E. G. Lundius, Ö. Baltekin, and J. Elf, “The synchronization of replication and division cycles in individual *E. coli* cells,” *Cell* **166**, 729 – 739 (2016).
- [21] I. Inoue, Y. Wakamoto, H. Moriguchi, K. Okano, and K. Yasuda, “On-chip culture system for observation of isolated individual cells,” *Lab Chip* **1**, 50–55 (2001).
- [22] Y. Wakamoto, J. Ramsden, and K. Yasuda, “Single-cell growth and division dynamics showing epigenetic correlations,” *The Analyst* **130**, 311–317 (2005).
- [23] M. Hashimoto, T. Nozoe, H. Nakaoka, R. Okura, S. Akiyoshi, K. Kaneko, E. Kussell, and Y. Wakamoto, “Noise-driven growth rate gain in clonal cellular populations,” *Proc. Natl. Acad. Sci. USA* **113**, 3251–3256 (2016).
- [24] M. Marucci, G. Ragnarsson, and A. Axelsson, “Electronic speckle pattern interferometry: A novel non-invasive tool for studying drug transport rate through free films,” *J. Control. Release.* **114**, 369 – 380 (2006).
- [25] D. Volfson, S. Cookson, J. Hasty, and L. S. Tsimring, “Biomechanical ordering of dense cell populations,” *Proc. Natl. Acad. Sci. USA* **105**, 15346–15351 (2008).
- [26] D. Boyer, W. Mather, O. Mondragón-Palomino, S. Orozco-Fuentes, T. Danino, J. Hasty, and L. S. Tsimring, “Buckling instability in ordered bacterial colonies,” *Phys. Biol.* **8**, 026008 (2011).
- [27] F. Si, B. Li, W. Margolin, and S. X. Sun, “Bacterial growth and form under mechanical compression,” *Sci. Rep.* **5**, 11367 (2016).
- [28] E. K. Chu, O. Kilic, H. Cho, A. Groisman, and A. Levchenko, “Self-induced mechanical stress can trigger biofilm formation in uropathogenic *Escherichia coli*,” *Nat. Commun.* **9** (2018), 10.1038/s41467-018-06552-z.
- [29] E. L. Bruger and C. M. Waters, “Bacterial quorum sensing stabilizes cooperation by optimizing growth strategies,” *Appl. Environ. Microbiol.* **82**, 6498–6506 (2016).
- [30] J. Ha, P. Hauk, K. Cho, Y. Eo, X. Ma, K. Stephens, S. Cha, M. Jeong, J. Suh, H. O. Sintim, W. E. Bentley, and K. Ryu, “Evidence of link between quorum sensing and sugar metabolism in *Escherichia coli* revealed via cocrystal structures of LsrK and HPr,” *Sci. Adv.* **4** (2018), 10.1126/sciadv.aar7063.
- [31] X. Carbonell, J. L. Corchero, R. Cubarsí, P. Vila, and A. Villaverde, “Control of *Escherichia coli* growth rate through cell density,” *Microbiol. Res.* **157**, 257 – 265 (2002).
- [32] R. M. Maier and I. L. Pepper, “Chapter 3 - bacterial growth,” in *Environmental Microbiology (Third Edition)*, edited by I. L. Pepper, C. P. Gerba, and T. J. Gentry (Academic Press, San Diego, 2015) third edition ed., pp. 37 – 56.
- [33] C. Chou, G. N. Bennett, and K. San, “Effect of Modulated Glucose Uptake on High-Level Recombinant Protein Production in a Dense *Escherichia coli* Culture,” *Biotechnol. Prog.* **10**, 644–647 (1994).
- [34] E. Rojas, J. A. Theriot, and K. C. Huang, “Response of *Escherichia coli* growth rate to osmotic shock,” *Proc. Natl. Acad. Sci. USA* **111**, 7807–7812 (2014).
- [35] L. K. Harris and J. A. Theriot, “Relative rates of surface and volume synthesis set bacterial cell size,” *Cell* **165**, 1479 – 1492 (2016).
- [36] We noticed oscillations of Sk in some cases, both experimentally [Fig. S3(d) and Fig. S4(d)] and numerically [Fig. S7(a) and Fig. S7(c)]. Numerically, we found that the oscillation disappears if we keep a constant number of cells, by eliminating one of the two daughter cells after each cell division. This led us to believe that those oscillations are due to strong correlation of cell cycles between sisters and close relatives.
- [37] The weak dependence of $F(x)$ on the environment is not contradictory to the result by Iyer-Biswas *et al.* [5, 7] that the size distribution of cells of a particular age is independent of the incubation temperature. Since the distribution of the cell ages may depend on the culture condition, our $F(x)$ is not necessarily independent of the environment.
- [38] J. Wakita, H. Kuninaka, T. Matsuyama, and M. Matushita, “Size distribution of bacterial cells in homogeneously spreading disk-like colonies by *Bacillus subtilis*,” *J. Phys. Soc. Jpn.* **79**, 094002 (2010).
- [39] F. Si, D. Li, S. E. Cox, John T. Sauls, Omid Azizi, Cindy Sou, Amy B. Schwartz, Michael J. Erickstad, Yonggun Jun, Xintian Li, and Suckjoon Jun, “Invariance of initiation mass and predictability of cell size in *Escherichia coli*,” *Curr. Biol.* **27**, 1278 – 1287 (2017).
- [40] G. Micali, J. Grilli, J. Marchi, M. Osella, and M. Cosentino Lagomarsino, “Dissecting the control mechanisms for DNA replication and cell division in *E. coli*,” *Cell Rep.* **25**, 761 – 771.e4 (2018).
- [41] G. Micali, J. Grilli, M. Osella, and M. Cosentino Lagomarsino, “Concurrent processes set *E. coli* cell division,” *Sci. Adv.* **4**, eaau3324 (2018).
- [42] F. Si, G. Le Treut, J. T. Sauls, S. Vadia, P. A. Levin, and S. Jun, “Mechanistic origin of cell-size control and homeostasis in bacteria,” *Curr. Biol.* **29**, 1760 – 1770.e7 (2019).
- [43] J. D. Wang and P. A. Levin, “Metabolism, cell growth and the bacterial cell cycle,” *Nat. Rev. Microbiol.* **7**, 822–827 (2009).
- [44] M. Campos, I. V. Surovtsev, S. Kato, A. Paintdakhi, B. Beltran, S. E. Ebmeier, and C. Jacobs-Wagner, “A constant size extension drives bacterial cell size homeostasis,” *Cell* **159**, 1433 – 1446 (2014).
- [45] S. Taheri-Araghi, S. Bradde, J. T. Sauls, N. S. Hill, P. A. Levin, J. Paulsson, M. Vergassola, and S. Jun, “Cell-size control and homeostasis in bacteria,” *Curr. Biol.* **25**, 385 – 391 (2015).
- [46] J. Monod, “The growth of bacterial cultures,” *Annu. Rev. Microbiol.* **3**, 371–394 (1949).

- [47] M. H. Buckstein, J. He, and H. Rubin, “Characterization of Nucleotide Pools as a Function of Physiological State in *Escherichia coli*,” *J. Bacteriol.* **190**, 718–726 (2008).
- [48] K. Sekar, R. Rusconi, J. T. Sauls, T. Fuhrer, E. Noor, J. Nguyen, V. I. Fernandez, M. F. Buffing, M. Berney, S. Jun, R. Stocker, and U. Sauer, “Synthesis and degradation of *ftsZ* quantitatively predict the first cell division in starved bacteria,” *Mol. Syst. Biol.* **14**, e8623 (2018).
- [49] James W. Sinko and William Streifer, “A model for population reproducing by fission,” *Ecology* **52**, 330–335 (1971).
- [50] O. Diekmann, H. A. Lauwerier, T. Aldenberg, and J. A. J. Metz, “Growth, fission and the stable size distribution,” *J. Math. Biol.* **18**, 135–148 (1983).
- [51] J. J. Tyson and O. Diekmann, “Sloppy size control of the cell division cycle,” *J. Theor. Biol.* **118**, 405–426 (1986).
- [52] L. Robert, M. Hoffmann, N. Krell, S. Aymerich, J. Robert, and M. Doumic, “Division in *Escherichia coli* is triggered by a size-sensing rather than a timing mechanism,” *BMC Biol.* **12** (2014), 10.1186/1741-7007-12-17.
- [53] K. Hosoda, T. Matsuura, H. Suzuki, and T. Yomo, “Origin of lognormal-like distributions with a common width in a growth and division process,” *Phys. Rev. E* **83**, 031118 (2011).
- [54] L. U. Magnusson, A. Farewell, and T. Nyström, “*ppgpp*: a global regulator in *escherichia coli*,” *Trends Microbiol.* **13**, 236–242 (2005).
- [55] D. J. Ferullo and S. T. Lovett, “The stringent response and cell cycle arrest in *escherichia coli*,” *PLoS Genet.* **4**, 1–15 (2008).
- [56] M. Bär, R. Großmann, S. Heidenreich, and F. Peruani, “Self-propelled rods: Insights and perspectives for active matter,” *Annu. Rev. Condens. Matter Phys.* **11** (2019), 10.1146/annurev-conmatphys-031119-050611.
- [57] A. Beer and G. Ariel, “A statistical physics view of swarming bacteria,” *Mov. Ecol.* **7** (2019), 10.1186/s40462-019-0153-9.
- [58] L. Hall-Stoodley, J. W. Costerton, and P. Stoodley, “Bacterial biofilms: from the natural environment to infectious diseases,” *Nat. Rev. Microbiol.* **2**, 95–108 (2004).
- [59] H. Boudarel, J. Mathias, B. Blaysat, and M. Grédiac, “Towards standardized mechanical characterization of microbial biofilms: analysis and critical review,” *NPJ Biofilms Microbiomes* **4** (2018), 10.1038/s41522-018-0062-5.
- [60] C. Fuqua, A. Filloux, J. Ghigo, and K. L. Visick, “Biofilms 2018: a diversity of microbes and mechanisms,” *J. Bacteriol.* **201**, e00118–19 (2019).
- [61] J. Grilli, M. Osella, A. S. Kennard, and M. Cosentino Lagomarsino, “Relevant parameters in models of cell division control,” *Phys. Rev. E* **95**, 032411 (2017).
- [62] C. Furusawa, T. Suzuki, A. Kashiwagi, T. Yomo, and K. Kaneko, “Ubiquity of log-normal distributions in intra-cellular reaction dynamics,” *Biophysics* **1**, 25–31 (2005).
- [63] H. Salman, N. Brenner, C. Tung, N. Elyahu, E. Stolovicki, L. Moore, A. Libchaber, and E. Braun, “Universal protein fluctuations in populations of microorganisms,” *Phys. Rev. Lett.* **108**, 238105 (2012).
- [64] S. Rulands, F. Lescroart, S. Chabab, C. J. Hindley, N. Prior, M. K. Sznurkowska, M. Huch, A. Philpott, C. Blanpain, and B. D. Simons, “Universality of clone dynamics during tissue development,” *Nat. Phys.* **14**, 469–474 (2018).
- [65] H. Nakaoka and Y. Wakamoto, “Aging, mortality, and the fast growth trade-off of *schizosaccharomyces pombe*,” *PLoS Biol.* **15**, 1–29 (2017).

Appendix D: Supplementary Table and Figures

TABLE S1. Culture conditions, ingredients and osmotic pressure.

Medium (Osmotic pressure [Osm/kg])	Ingredients	Concentration
LB broth (Millar) (0.38)	Tryptone	1 wt%
	Sodium Chloride	1 wt%
	Yeast extract	0.5 wt%
M9(Glc+a.a.) medium (0.21)	Disodium Phosphate (Anhydrous)	0.68 wt%
	Monopotassium Phosphate	0.3 wt%
	Sodium Chloride	0.05 wt%
	Ammonium Chloride	0.1 wt%
	Magnesium Phosphate	2 mM
	Calcium Chloride	0.1 mM
	Glucose	0.2 wt%
	MEM Amino Acids solution (M5550, Sigma)	1 wt%
M9(Glc) medium (0.22)	Disodium Phosphate (Anhydrous)	0.68 wt%
	Monopotassium Phosphate	0.3 wt%
	Sodium Chloride	0.05 wt%
	Ammonium Chloride	0.1 wt%
	Magnesium Phosphate	2 mM
	Calcium Chloride	0.1 mM
	Glucose	0.2 wt%
M9(α MG) medium (0.21)	Disodium Phosphate (Anhydrous)	0.68 wt%
	Monopotassium Phosphate	0.3 wt%
	Sodium Chloride	0.05 wt%
	Ammonium Chloride	0.1 wt%
	Magnesium Phosphate	2 mM
	Calcium Chloride	0.1 mM
	Alpha-methyl-D-glucoopyranoside.	0.2 wt%
TB medium (0.21)	Tryptone	1 wt%
	Sodium Chloride	0.5 wt%
PBS(-) (0.27)	Potassium Dihydrogenphosphate	0.02 wt%
	Disodium phosphate (Anhydrous)	0.115 wt%
	Potassium Chloride	0.02 wt%
	Sodium Chloride	0.8 wt%

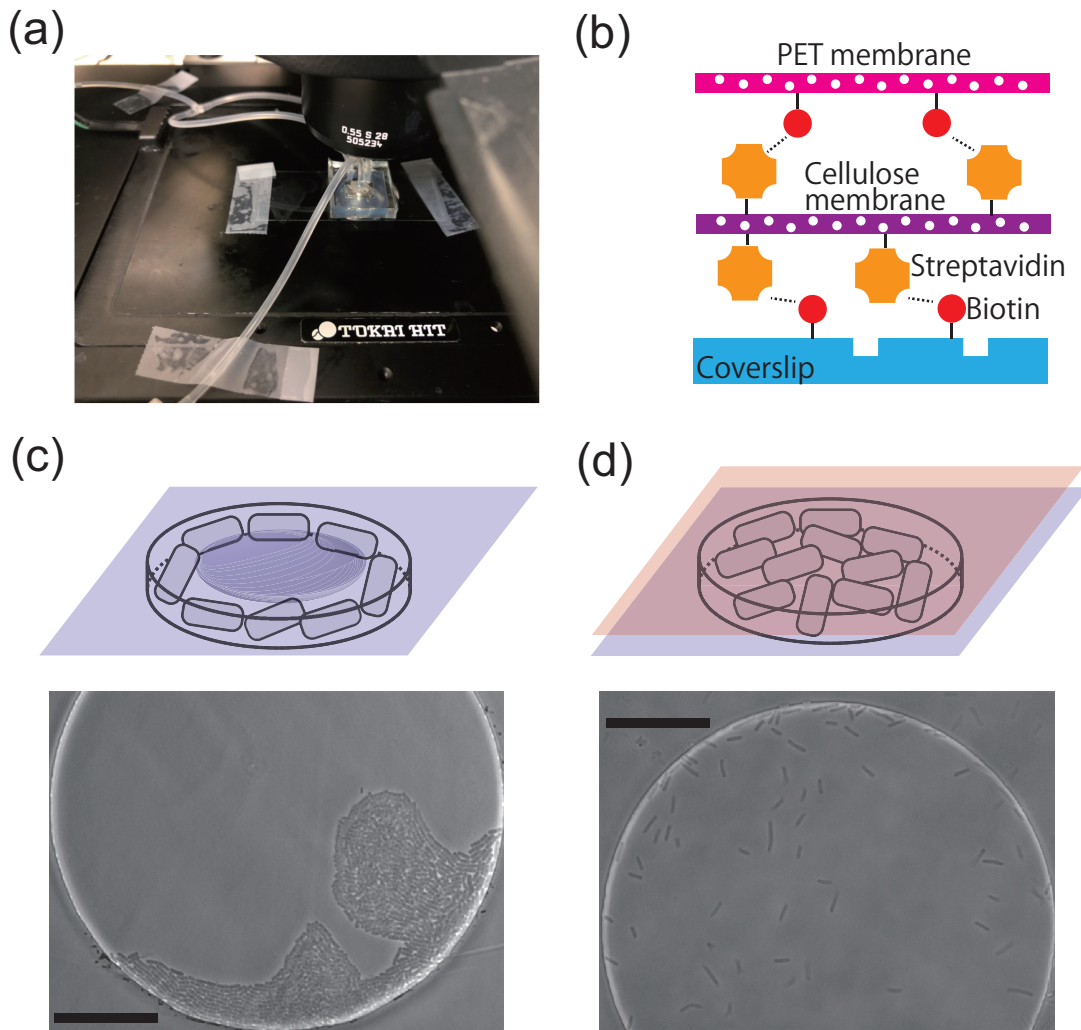


FIG. S1. Supplementary figures on the setup of the EMPS. (a) Photograph of the device mounted on the microscope stage. The coverslip and tubes are fixed to the stage by mending tapes. (b) Illustration of the chemical bonding between a bilayer membrane and a glass coverslip. A streptavidin-decorated cellulose membrane is sandwiched by a biotin-coated PET membrane and coverslip. (c)(top) Sketch of growth of bacterial cells inside a circular well covered only by a cellulose membrane. Since the membrane bends and presses cell beneath, cells do not swim but form clusters, extending toward the wall. (bottom) Photograph of motile *E. coli* RP437 in a well (diameter $110\ \mu\text{m}$, depth $1.1\ \mu\text{m}$) covered only by a cellulose membrane. TB medium was constantly supplied at $37\ ^\circ\text{C}$ (see Materials and Methods for details). Despite the motility, cells were confined near the wall and unable to swim freely (see also Movie S1). The scale bar is $30\ \mu\text{m}$. (d)(top) Sketch of growth of cells inside a well covered by a PET-cellulose bilayer membrane. The rigid bilayer membrane is sustained without bending, leaving a sufficient gap beneath for cells. (bottom) Photograph of motile *E. coli* RP437 in a well (same diameter and depth as in ((c), bottom) covered by a bilayer membrane. Cells were able to swim freely (see also Movie S2). Growth conditions are same as in ((c), bottom).

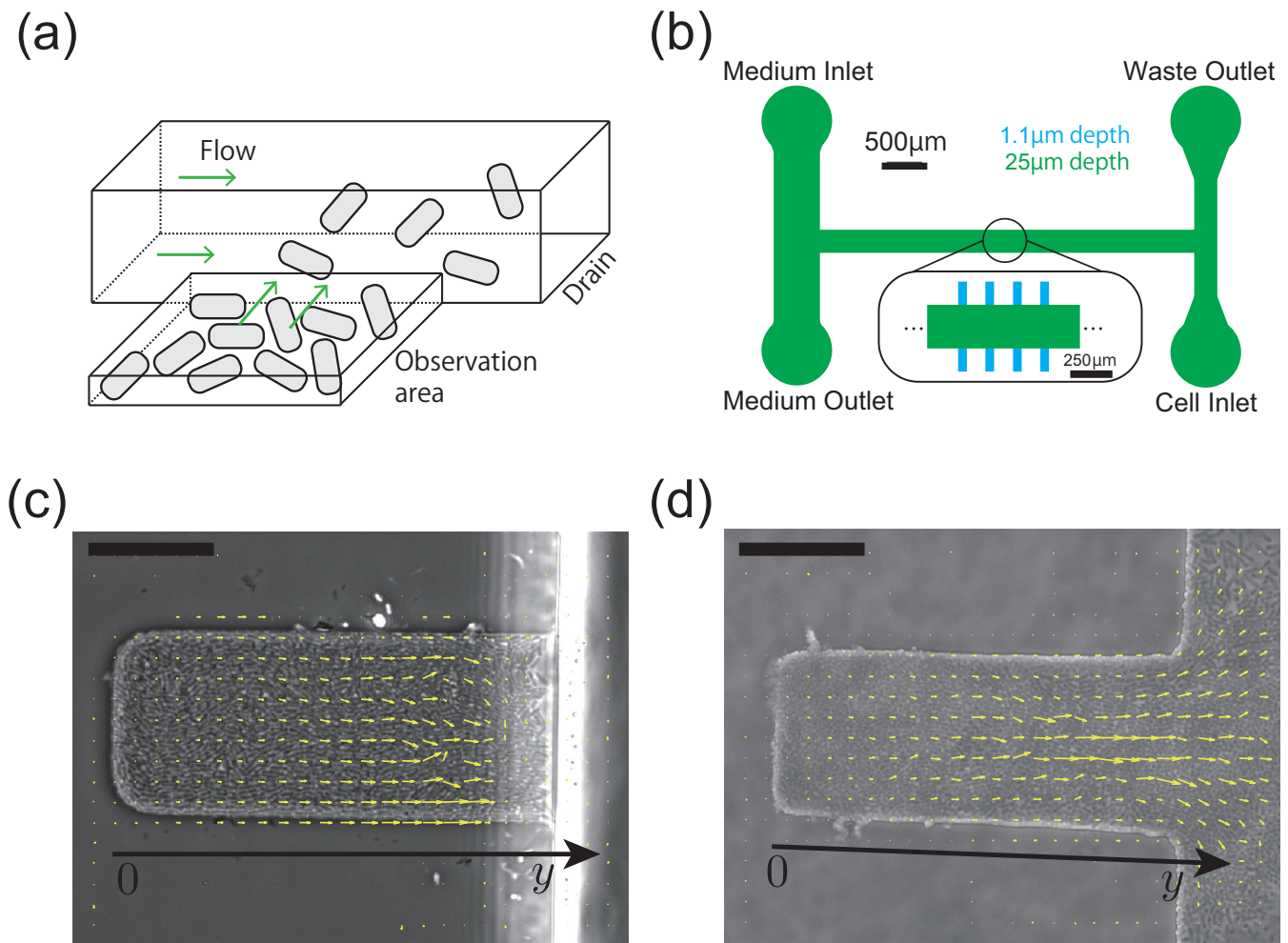


FIG. S2. Supplementary figures on the cell growth measurement. (a) Sketch of the design of microchannels in the PDMS-based device. Medium flow in the drain channel removes cells expelled from the observation area (trap). Nutrient is supplied to the cells inside the trap via diffusion from the drain channel. (b) The design of the PDMS-based device. The green region corresponds to the drain channel, and the blue regions are the U-shape traps. (c) Top view of the trap (30 μm wide, 88 μm long, 1.1 μm deep) in the PDMS-based device. The trap is filled with *E. coli* W3110 ΔfliC Δflu ΔfimA . The yellow arrows represent the velocity field of flow driven by cell proliferation, measured by particle image velocimetry (PIV). The scale bar is 25 μm . See also Movie S3. (d) Top view of the trap (30 μm wide, 80 μm long, 1.0 μm deep) in the EMPS. See also Movie S4.

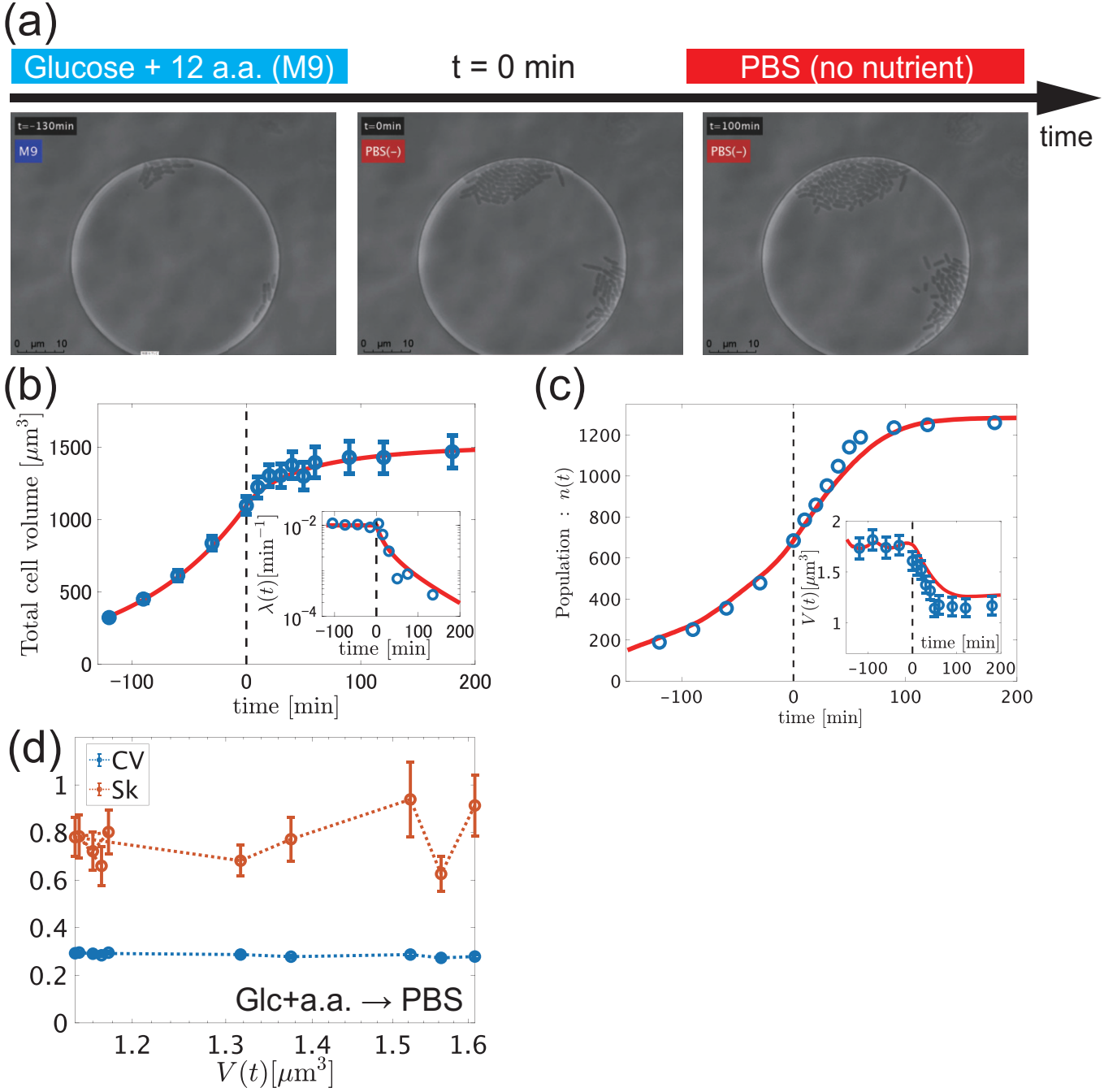


FIG. S3. Results from the observations of reductive division in the case of M9(Glc+a.a.) \rightarrow PBS. The data were collected from 17 wells. (a) Snapshots taken during the reductive division process. See also Movie S8. (b),(c) Experimental data (blue symbols) for the total cell volume $V_{\text{tot}}(t)$ (b), the growth rate $\lambda(t)$ ((b), Inset), the number of the cells $n(t)$ (c) and the mean cell volume $V(t)$ ((c), Inset) in the case of M9(Glc) \rightarrow PBS, compared with the simulation results (red curves). The error bars indicate segmentation uncertainty in the image analysis (see Appendix A 8). $t = 0$ is the time at which PBS entered the device (black dashed line). (d) CV and Sk [Eq.(3)] against $V(t) = \langle v \rangle$. The error bars were estimated by the bootstrap method with 1000 realizations.

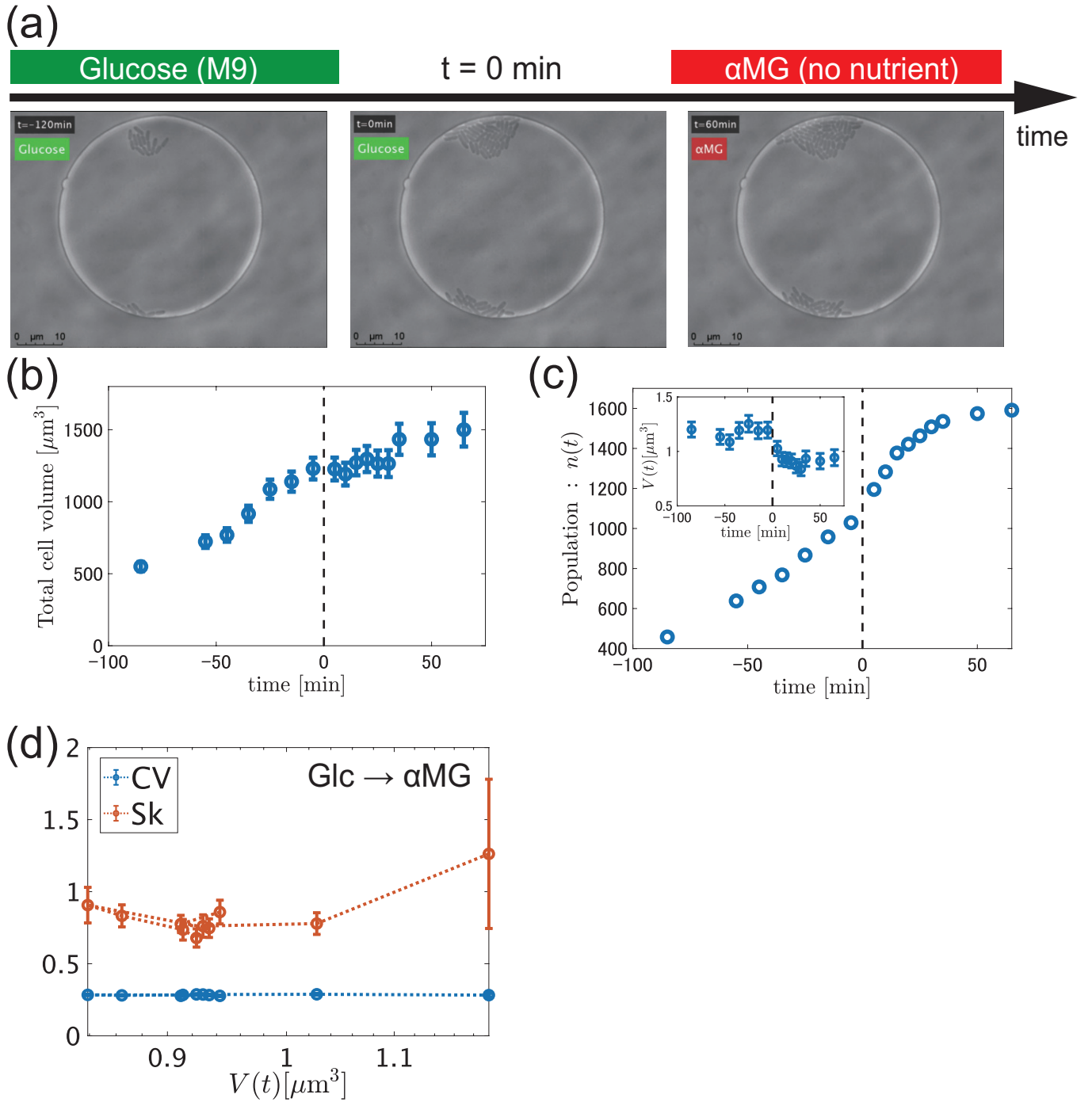


FIG. S4. Results from the observations of reductive division in the case of $\text{M9}(\text{Glc}) \rightarrow \text{M9}(\alpha\text{MG})$. The data were collected from 26 wells. (a) Snapshots taken during the reductive division process. See also Movie S9. (b),(c) Experimental data for the total cell volume $V_{\text{tot}}(t)$ (b), the number of the cells $n(t)$ (c) and the mean cell volume $V(t)$ ((c), Inset) in the case of $\text{M9}(\text{Glc}) \rightarrow \text{M9}(\alpha\text{MG})$. The error bars indicate segmentation uncertainty in the image analysis (see Appendix A 8). $t = 0$ is the time at which αMG entered the device (black dashed line). (d) CV and Sk [Eq.(3)] against $V(t) = \langle v \rangle$. The error bars were estimated by the bootstrap method with 1000 realizations.

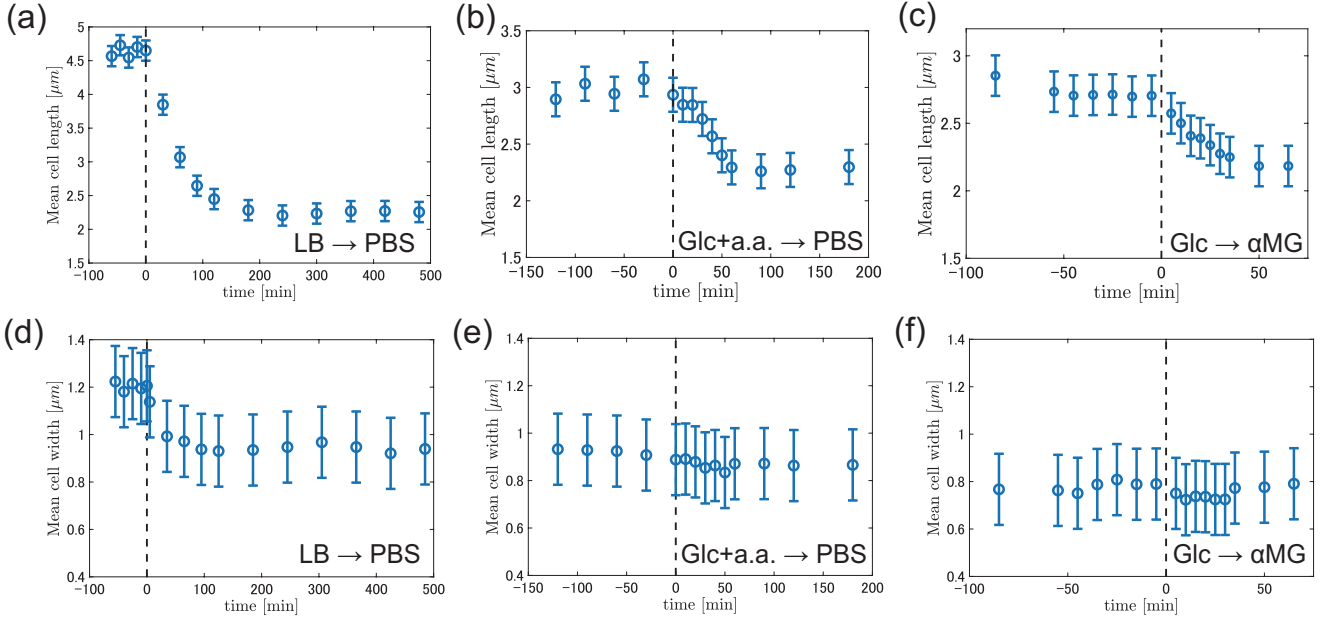


FIG. S5. Time series of the mean cell length and the mean cell width during the starvation process. $t = 0$ is the time at which the non-nutritious buffer entered the device (black dashed line). (a),(b),(c) Time series of the mean cell length in the case of LB \rightarrow PBS (a), M9(Glc+a.a.) \rightarrow PBS (b) and M9(Glc) \rightarrow M9(α MG) (c). The error bars indicate segmentation uncertainty in the image analysis (see Appendix A 8). (d),(e),(f) Time series of the mean cell width in the case of LB \rightarrow PBS (d), M9(Glc+a.a.) \rightarrow PBS (e) and M9(Glc) \rightarrow M9(α MG) (f). The error bars indicate segmentation uncertainty in the image analysis.

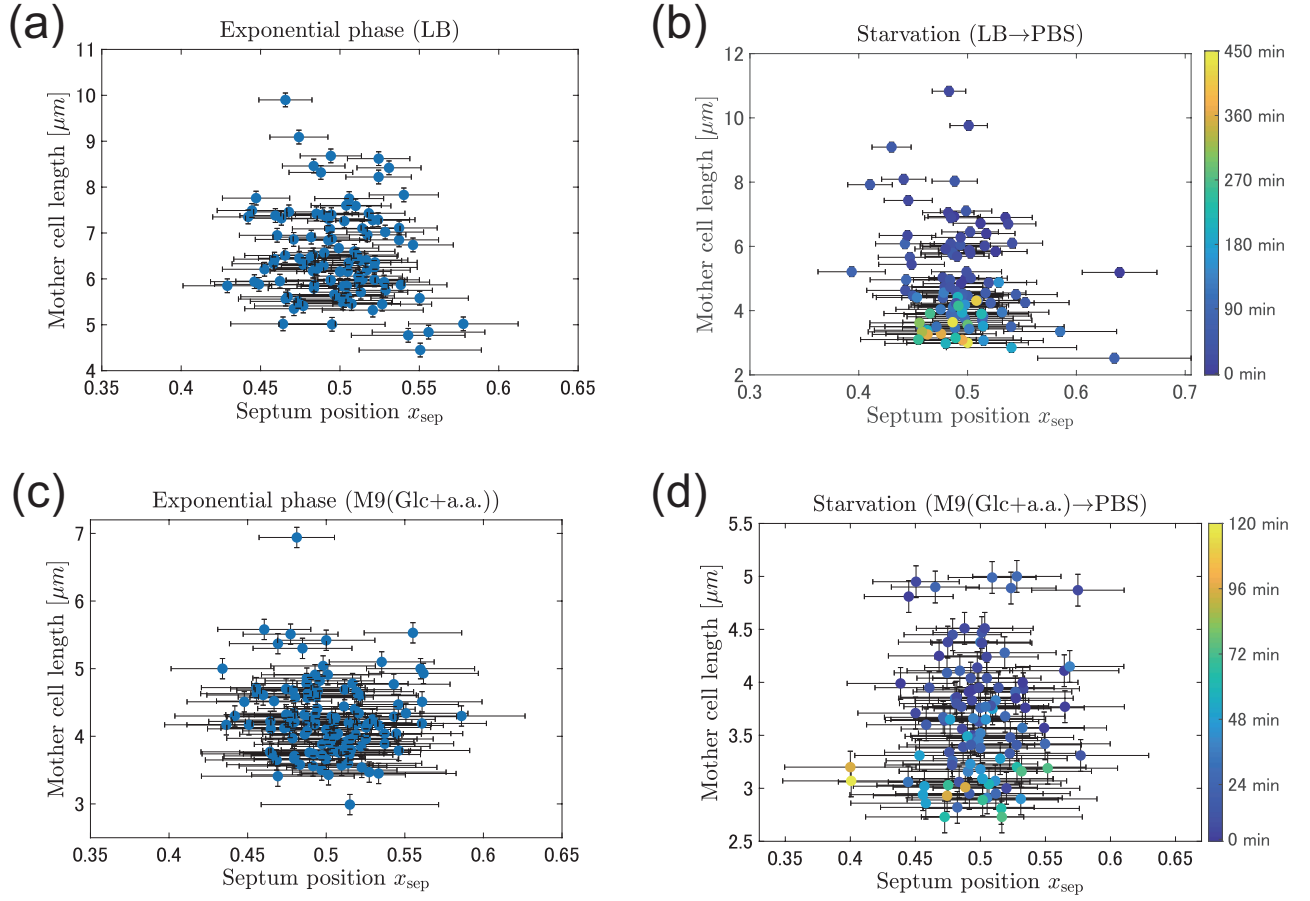


FIG. S6. Cell-to-cell fluctuations of the septum position. Scatter plots of the mother cell length against the septum position x^{sep} are shown for four different cases. The data were taken from more than 100 cell division events chosen randomly for each case. The error bars indicate segmentation error in the image analysis. There is no visible correlation between the mother cell size and the standard deviation of the septum position. (a) Scatter plot for the exponential growth phase in LB broth. The standard deviation of the septum position is $x_{\text{std}}^{\text{sep}} = 0.028$. (b) Scatter plot during the starvation process for LB \rightarrow PBS. The color represents the time passed since PBS entered the device. The standard deviation of the septum position is $x_{\text{std}}^{\text{sep}} = 0.036$. (c) Scatter plot for the exponential growth phase in M9(Glc+a.a.) medium. The standard deviation of the septum position is $x_{\text{std}}^{\text{sep}} = 0.029$. (d) Scatter plot during the starvation process for M9(Glc+a.a.) \rightarrow PBS. The standard deviation of the septum position is $x_{\text{std}}^{\text{sep}} = 0.032$.

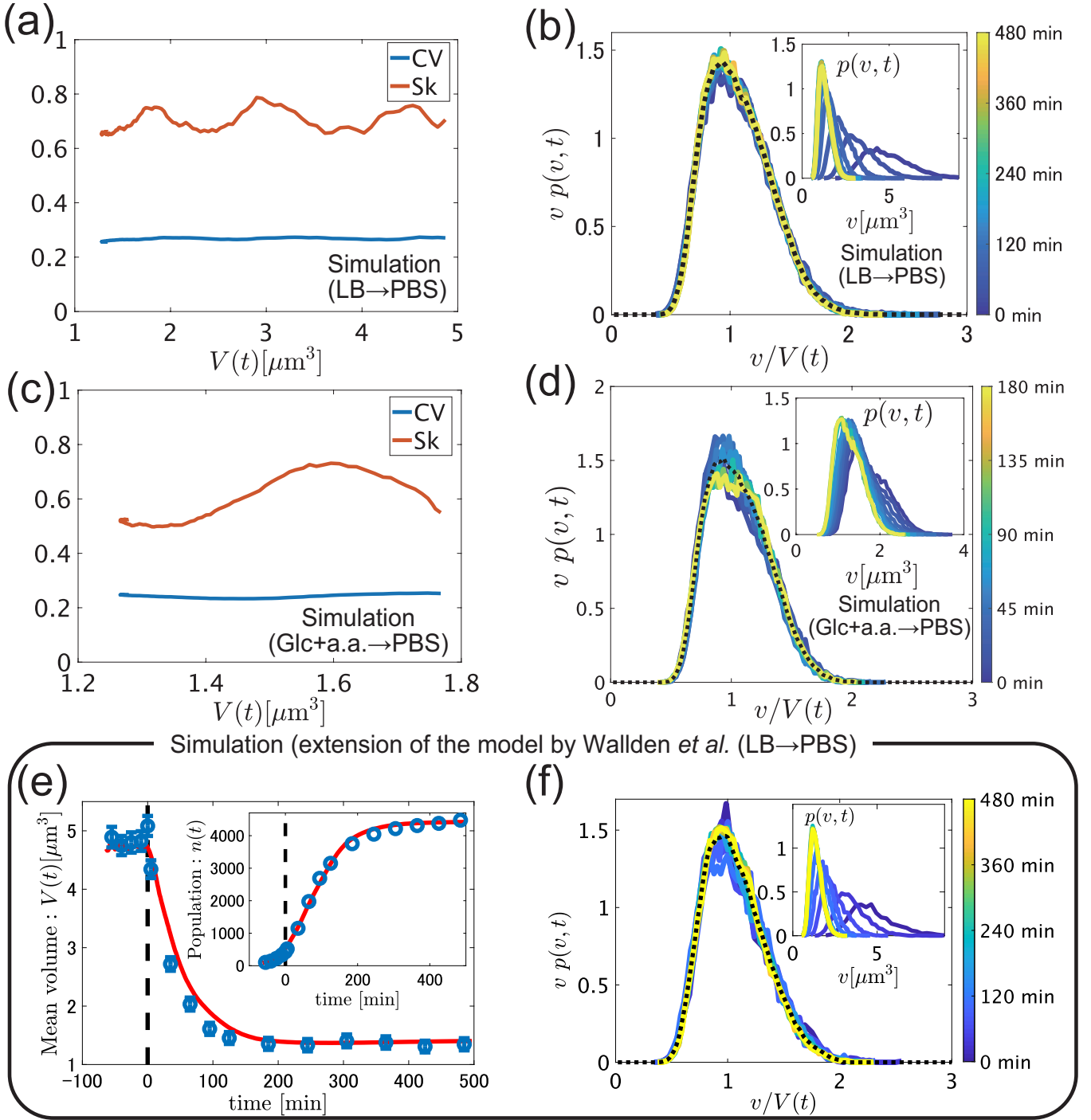


FIG. S7. Supplementary figures on the simulation results. (a) CV and Sk [Eq. (3)] against $V(t) = \langle v \rangle$ in the model for LB \rightarrow PBS. The error bars estimated by the bootstrap method with 1000 realizations were smaller than the symbol size. The oscillation of Sk disappears if we keep a constant number of cells, by eliminating one of the two daughter cells after each cell division. This led us to believe that those oscillations are due to strong correlation of cell cycles between sisters and close relatives. (b) Overlapping of the rescaled cell size distributions during starvation in the model for LB \rightarrow PBS (the same figure as Fig. 6(c)). The dashed line represents the time average of the datasets. (Inset) The non-rescaled cell size distributions at $t = 0, 5, 30, 60, 90, 120, 180, 240, 300, 360, 420, 480$ min from right to left. (c) CV and Sk [Eq. (3)] against $V(t) = \langle v \rangle$ in the model for M9(Glc+a.a.) \rightarrow PBS. The error bars estimated by the bootstrap method with 1000 realizations were smaller than the symbol size. (d) Overlapping of the rescaled cell size distributions during starvation in the model for M9(Glc+a.a.) \rightarrow PBS. (Inset) The non-rescaled cell size distributions at $t = 0, 10, 20, 30, 40, 50, 60, 90, 120, 180$ min from right to left. (e) Comparison of the experiment (LB \rightarrow PBS) and simulation based on the model by Wallden *et al.* (LB \rightarrow PBS). (f) Overlapping of the rescaled cell size distributions during starvation in simulation based on the model by Wallden *et al.* (LB \rightarrow PBS). (Inset) The non-rescaled cell size distributions at $t = 0, 5, 30, 60, 90, 120, 180, 240, 300, 360, 420, 480$ min from right to left.

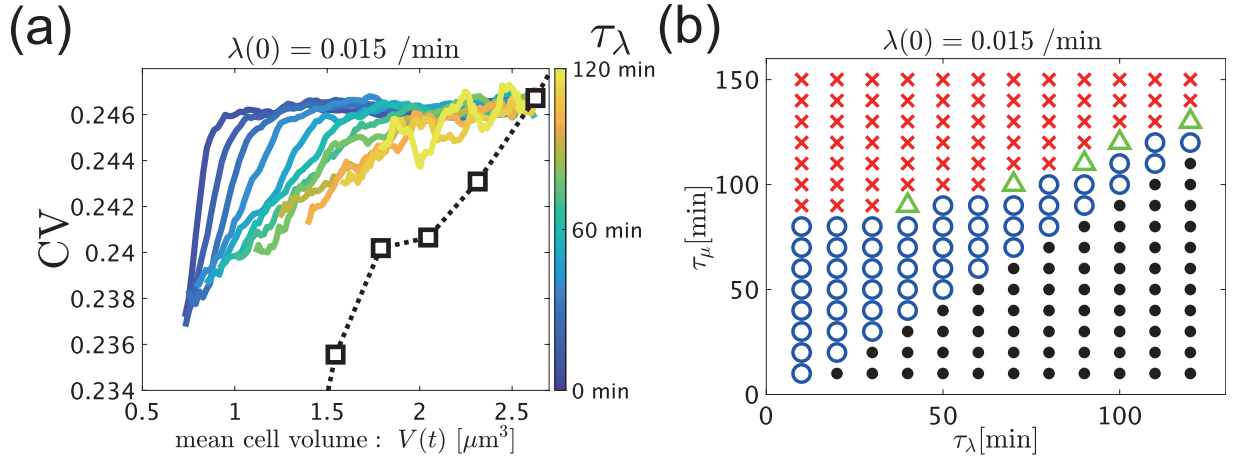


FIG. S8. Supplementary numerical results on the range of validity of the scale invariance. The initial growth rate is fixed at $\lambda(0) = 0.015$ /min unless otherwise stipulated. (a) The master curves of the $\langle v \rangle$ -CV trajectories for different τ_λ . Those are obtained by taking the average of the CV values at each $\langle v \rangle$ over different $\tau_\mu (> \tau_\lambda)$. τ_λ ranges from 10 to 120 min. The black squares represent the states in steady growth conditions with the growth rate $\lambda(0)$ ranging from 0.005 to 0.015 /min. (b) Phase diagram. \times : the scale invariance breaks down. Blue \circ : the scale invariance holds. Green \triangle : near the boundary. Black dots: the scale invariance holds but the mean volume increases.

Appendix E: Supplementary movie descriptions

Movie S1:

Growth of motile *E. coli* RP437 inside a well covered only by a cellulose membrane. The diameter of the well is $110\ \mu\text{m}$, and the depth is $1.1\ \mu\text{m}$. Being pressed by the bent cellulose membrane, cells do not swim but form clusters, extending toward the wall. The movie is played at $600\times$ real-time speed.

Movie S2:

Growth of motile *E. coli* RP437 inside a well covered by a PET-cellulose bilayer membrane. The diameter of the well is $110\ \mu\text{m}$, and the depth is $1.1\ \mu\text{m}$. Cells freely swim inside the quasi-two-dimensional well. The movie is played at real-time speed.

Movie S3:

Coherent flow of non-motile bacterial cells driven by self-replication in a U-shape trap of the PDMS-based device. The trap is $30\ \mu\text{m}$ wide, $88\ \mu\text{m}$ long, and $1.1\ \mu\text{m}$ deep. *E. coli* strain W3110 $\Delta\text{fliC}\ \Delta\text{flu}\ \Delta\text{fimA}$ is used.

Movie S4:

Coherent flow of non-motile bacterial cells driven by self-replication in a U-shape trap of the EMPS. The trap is $30\ \mu\text{m}$ wide, $80\ \mu\text{m}$ long, and $1.0\ \mu\text{m}$ deep. *E. coli* strain W3110 $\Delta\text{fliC}\ \Delta\text{flu}\ \Delta\text{fimA}$ is used.

Movie S5:

A cross-sectional movie of the EMPS, recorded while medium is switched from transparent PBS to a PBS solution of $10\ \mu\text{M}$ rhodamine. The diameter of the well is $45\ \mu\text{m}$ and the depth is $1.1\ \mu\text{m}$. A few non-motile *E. coli* (W3110 $\Delta\text{fliC}\ \Delta\text{flu}\ \Delta\text{fimA}$) are present in the well. The rhodamine solution flowed at a constant speed of approximately $6\ \text{mm/sec}$ above the membrane (flow rate $60\ \text{ml/hr}$). The movie is played at $19\times$ real-time speed.

Movie S6:

A cross-sectional movie of the EMPS, recorded while medium is switched from a PBS solution of $10\ \mu\text{M}$ rhodamine to transparent PBS. The diameter of the well is $45\ \mu\text{m}$ and the depth is $1.1\ \mu\text{m}$. A few non-motile *E. coli* (W3110 $\Delta\text{fliC}\ \Delta\text{flu}\ \Delta\text{fimA}$) are present in the well. The PBS without rhodamine flowed at a constant speed of approximately $6\ \text{mm/sec}$ above the membrane (flow rate $60\ \text{ml/hr}$). The movie is played at $19\times$ real-time speed.

Movie S7:

Reductive division of *E. coli* MG1655 for the case $\text{LB} \rightarrow \text{PBS}$. The diameter of the well is $55\ \mu\text{m}$ and the depth is $0.8\ \mu\text{m}$. Until $t = 0$, fresh LB broth was supplied at a constant flow speed of approximately $0.2\ \text{mm/sec}$ above the membrane (flow rate $2\ \text{ml/hr}$). PBS entered the device at $t = 0$ and quickly replaced the LB broth, by setting a high flow speed $\sim 6\ \text{mm/sec}$ ($60\ \text{ml/hr}$) until $t = 5\ \text{min}$. After flushing, we continued supplying PBS at the flow speed of approximately $0.2\ \text{mm/sec}$ ($2\ \text{ml/hr}$).

Movie S8:

Reductive division of *E. coli* MG1655 for the case $\text{M9}(\text{Glc}+\text{a.a.}) \rightarrow \text{PBS}$. The diameter of the well is $55\ \mu\text{m}$ and the depth is $0.8\ \mu\text{m}$. PBS entered the device at $t = 0$. The flow rates were controlled and set in the same manner as for Movie S7.

Movie S9:

Reductive division of *E. coli* MG1655 for the case $\text{M9}(\text{Glc}) \rightarrow \text{M9}(\alpha\text{MG})$. The diameter of the well is $55\ \mu\text{m}$ and the depth is $0.8\ \mu\text{m}$. $\text{M9}(\alpha\text{MG})$ entered the device at $t = 0$. The flow rates were controlled and set in the same manner as for Movie S7.